Quaternary Science Reviews 250 (2020) 106641

Contents lists available at ScienceDirect

Quaternary Science Reviews

journal homepage: www.elsevier.com/locate/quascirev

Abrupt last glacial dust fall over southeast England associated with dynamics of the British-Irish ice sheet

Thomas Stevens [a, *], Daniele Sechi [b], Balázs Bradák [c], Ragna Orbe [a], Yunus Baykal [a], Giulia Cossu [b], Charilaos Tziavaras [a], Stefano Andreucci [d], Vincenzo Pascucci [b, e]

[a] Department of Earth Sciences, Uppsala University, Villavägen 16, Uppsala, 75236, Sweden
[b] Department of Architecture, Design and Planning, University of Sassari, Piazza Duomo 6, I-07041, Alghero (SS), Italy
[c] Department of Physics, University of Burgos, Av. De Cantabria s/n, 09006, Burgos, Spain
[d] Dipartimento di Scienze Chimiche e Geologiche, Università degli Studi di Cagliari, Cittadella Universitaria (Blocco A), Monserrato, 09127, CA, Italy
[e] Institute of Geology and Petroleum Technologies, Kazan Federal University, Kazzan, Russia

ARTICLE INFO

Article history:
Received 12 May 2020
Received in revised form
24 September 2020
Accepted 6 October 2020
Available online 24 October 2020

Keywords:
Loess
Pegwell bay
Luminescence
Multi-proxy
Brickearth
Palaeoenvironment

ABSTRACT

Loess deposits in southern Britain contain a record of dust, climate and landscape dynamics over the last glacial, yet their age and accumulation rate remain poorly known. Furthermore, the environmental controls on the loess-soil stratigraphy shown in the thickest deposits in southeast England are still debated. Here we apply the first high sampling resolution quartz optically stimulated luminescence study of dust accumulation and loess formation in Britain at the Pegwell Bay site in east Kent. We couple this to mineral magnetic, particle size and geochemical analyses to understand climate, environment and post depositional modification of the loess. The luminescence ages and Bayesian age modelling results suggest two phases of greatly enhanced dust accumulation at the site. Loess began to accumulate around c. 25–23.5 ka, coinciding with Heinrich event 2, and after subsequent lower accumulation rates, a second enhanced phase of deposition occurred at around 20–19 ka. We propose a model where the dynamics of the British-Irish and Fennoscandian Ice Sheets, associated glacial lake drainage, and linked reorganisations of atmospheric circulation, all controlled loess accumulation in southern Britain. Accumulation in the first phase was triggered by increased sediment supply from initial retreat of the North Sea ice lobe, and drainage of Dogger Lake. Loess accumulation during this phase was enhanced by easterly winds from Atlantic depressions tracking to the south of Britain, caused by the maximum extent of the Irish Sea Ice Stream at c. 25–24 ka. The subsequent retreat of the western part of the British Irish Ice Sheet then allowed storm tracking further north, which reduced effectiveness of dust transporting winds across southern Britain, while sediment supply and availability was reduced in North Sea source areas. A second retreat of the maximum extent of the North Sea Lobe of ice after c. 21–20 ka would have led to another abrupt input of sediment-rich ice dammed lake and meltwater from eastern England and the North Sea into the exposed southern North Sea area. This would have again dramatically increased sediment availability for transport and deposition as loess in SE England, resulting in the second dust accumulation phase. We also propose that the abrupt stratigraphic change from calcareous to non-calcareous loess up section at Pegwell Bay was driven, not by these changes in dust input, but rather deepening of the permafrost active layer after c. 21 ka. This deepening was associated with warmer and wetter conditions driven by Atlantic storms tracking further north following the regression of the Irish Sea Ice Stream and overall ice sheet retreat. As such, last glacial dust dynamics and loess accumulation in Britain is highly influenced by the interaction of the British Irish Ice Sheet the Fennoscandian Ice sheet, Atlantic storm tracks, and the topography and drainage of the exposed North Sea.

1. Introduction

Southern Britain is draped in a thin cover of loess, loess derivatives, and loessic soils (Catt, 1978) (Fig. 1). While non-reworked

* Corresponding author.
E-mail address: thomas.stevens@geo.uu.se (T. Stevens).

https://doi.org/10.1016/j.quascirev.2020.106641

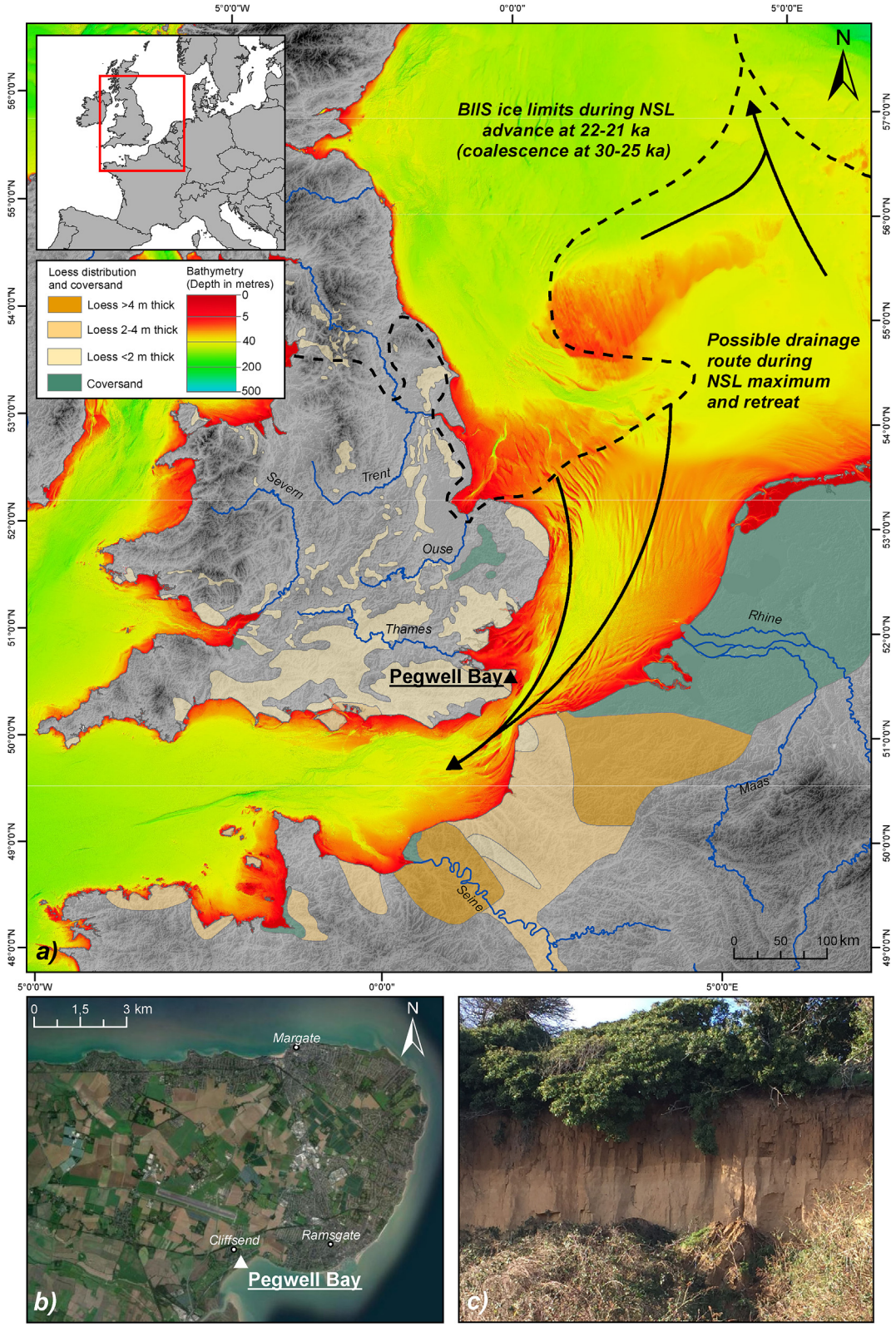

Fig. 1. Site location and context. A) Map of loess and coversand distribution in NW Europe and southern Britain (based on Catt, 1977; Antoine et al., 2003; Bateman and Catt 2007), with Pegwell Bay noted. Also shown are approximate British-Irish and Fennnoscandian ice sheet limits at c. 22–21 ka, around the time of peak North Sea Lobe extent and drainage of glacial lake Dogger (based on Roberts et al., 2018). Possible North Sea drainage routes are shown by black arrows. Bathymetry of the North Sea and English Channel are downloaded from EMODnet; SRTM data downloaded from CGIARCSI and hillslope shading is applied to topography to increase visibility. Inset map shows area in wider context. (shapefile credits: EEA; thematicmapping.org; tapiquen-sig.jimdofree.com. Carlos Efraín Porto Tapiquén. Geografía, SIG y Cartografía Digital. Valencia, Spain, 2020). B) Aerial photograph of the area around Pegwell Bay site showing site location at the former hover port at Cliffs End. C) Photograph of sampled section. Base map A) and aerial photograph B) were generated in Arcgis (Esri, DigitalGlobe, GeoEye, Earthstar Geographics, CNES/Airbus DS, USDA, USGS, AeroGRID, IGN, and the GIS User Community).

loess is rare, relatively thick (potentially up to 8 m) apparently in situ aeolian loess deposits are concentrated in southeast England, particularly surrounding the Thames Estuary (Catt, 1978 Northmore et al., 1996). Many of these deposits have previously been categorized as 'brickearth', a term reflecting the use of a certain type of silty sediment in brick manufacturing (Loveday, 1962), but which also covers a range of non-loessic sediment. The precise origin of these loess deposits remains debated (Bateman and Catt, 2007; Smalley et al., 2009), and their age only generally known (Wintle, 1981; Parks and Rendell, 1992; Clarke et al., 2007). Furthermore, the potential of these deposits as archives of dust activity and climate change has not yet been explored.

Loess deposits comprise pedogenetically altered wind-blown atmospheric mineral dust (Schaetzl et al., 2018). Atmospheric mineral dust is a major component of the climate system, affecting and responding to climate change via a number of complex feedbacks involving nutrient cycling, albedo, radiative forcing and cloud formation (Bullard et al., 2016). Despite this importance, understanding of past changes in dust activity is limited, largely due to the absence of suitably dated geological archives of dust over large areas (e.g., Albani et al., 2015). In particular, 'coarse dust' (>5 μm) particles, which have specific climate impacts and considerations, have been underestimated in terms of extent, influence and impact (Adebiye and Kok, 2020). As loess is dominantly comprised of coarse dust, it is an excellent archive of past variations in this material. However, the timing and rate of loess deposition is essential to constrain in order to utilise loess for understanding past coarse dust activity.

Loess in southeast England has been dated to approximately the last glacial using a variety of now mostly superseded luminescence methods (Wintle, 1981; Gibbard et al., 1987; Parks and Rendell, 1992; Clarke et al., 2007). While valuable for approximate age estimates, these previously obtained ages need testing with modern approaches (Roberts, 2008). Furthermore, the detailed independent dating that would elucidate the start and end, temporal continuity, and variability of dust deposition rates in England, has not yet been undertaken. Late Quaternary dust activity is especially important to understand due to widespread evidence for enhanced dustiness over this phase (Antoine et al., 2009; Rasmussen et al., 2014; Kang et al., 2015; Stevens et al., 2016; Moine et al., 2017; Újvári et al., 2017) and the likely associated significant climate impact (Claquin et al., 2003). Loess records from Western and Northern Europe also point to increased loess deposition during the latter part of the last glacial (Antoine et al., 2009) and evidence from the detailed Eifel lake sediments in Northwest Germany further reinforces an unusually dusty period at that time (Seelos et al., 2009). However, evidence constraining the timing of peak dustiness further north and west is limited.

1.1. Loess in southern England, the exposed North Sea, and European Ice Sheets

Exposed sediment in the Channel and North Sea has been proposed as a dust source for central, northern and western European loess (Fig. 1) (Sima et al., 2009), with transport driven by westerly depression tracks along the Channel during the last glacial (Antoine et al., 2009). Combined with extensive loose silt-size sediment availability, these depressions would have driven extensive dust storm activity and contributed to loess build up in France and Germany by westerly winds. As they tracked along the Channel, these same storms are proposed to have caused easterly flow in Southern Britain, and a North Sea/Channel source for loess in southern England is supported by heavy mineral assemblages and the general thinning of deposits and finer grain size distributions from Kent to East Devon, east to west (Catt, 1978; Catt and Staines, 1982). However, in north western France, katabatic winds have been suggested to be responsible for loess accumulation (Lefort et al., 2019), and polar easterlies are also potential candidates for dust transporting winds (Schaffernicht et al., 2020).

Crucially, and despite being proposed as a source of southern English loess by some authors (Catt and Staines, 1982; Bateman and Catt, 2007), the specific influence of the British Irish Ice Sheet (BIIS) on dust accumulation via changing drainage and sediment supply to the North Sea remains unclear. While sub-glacial grinding under the Fennoscandian and Alpine ice sheets is likely to have provided extensive sources of dust for loess deposits in large areas of Central and Eastern Europe (Újvári et al., 2012; Nawrocki et al., 2018), the influence of the BIIS on dustiness in Western Europe has not been considered in detail, and some authors rather suggest an Alpine provenance for loess in southern Britain (and by extension, sediment in the southern North Sea) (Smalley et al., 2009). However, heavy mineral assemblages and particle size data from loess in Britain suggest a genetic link with BIIS sediment sources (Catt and Staines, 1982). Loess in eastern and south eastern England has a mineralogical signature close to last glacial tills of eastern England (Bateman and Catt, 2007). By contrast, loess on the Lizard Peninsula and Isles of Scilly in southwest Britain shows mineralogical affinity to tills derived from the Irish Sea Ice Stream (Catt and Staines, 1982; Scourse, 1991). While there is a general westward fining of loess deposits along southern England, as far as East Devon, these western deposits become dramatically coarser, indicating derivation from western parts of the BIIS (Scourse, 1991).

Although the exact timing is uncertain, the BIIS and Fennoscandian Ice Sheet (FIS) likely converged in the North Sea Basin during the last glacial phase around 30–25 ka (Roberts et al., 2018), with the North Sea Lobe (NSL) of the BIIS showing extremely dynamic advance and retreat behaviour (Roberts et al., 2018; Evans et al., 2019). The NSL surged and reached the north Norfolk coast around 25 ka, and again at 22–21 ka (Fig. 1), potentially (Bullard et al., 2016) driven first by initial drainage of glacial lake Dogger, and then by its full drainage and decoupling of the Fennoscandian and British-Irish Ice Sheets (Roberts et al., 2018). These NSL advance events led to extensive formation of ice-dammed lakes over Eastern England and were followed by a highly dynamic and oscillatory retreat pattern (Evans et al., 2019). South of the NSL and Dogger Lake, the North Sea Basin would have been largely dry, with extensive fluvial and glaciofluvial systems draining the BIIS, FIS and Alpine ice sheet flowing south and southwest via the Channel River, or north into ice dammed lakes (Patton et al., 2017) (Fig. 1). The drainage of these glacial lakes and large-scale melting of parts of the FIS and BIIS are suggested to have led to major pulses of meltwater to the southern North Sea and Channel (Toucanne et al., 2015), dramatically reshaping the topography of the exposed North Sea (García-Moreno, 2017; De Clercq, 2018) and likely bringing extensive volumes of sediment into the area.

The last glacial is also a period of extreme climate oscillations, centred on the North Atlantic (Rasmussen et al., 2014), with abrupt stadial and interstadial oscillations recorded in Greenland ice cores and massive iceberg discharge occurring periodically during Heinrich events (Heinrich, 1988). It is unclear how much these oscillations will have affected, or been driven by, the BIIS (Knutz et al., 2001, 2002; Peck et al., 2006, 2007; Hibbert et al., 2009; Scourse et al., 2009; Haapaniemi et al., 2010), as well as the impact of these events on dustiness over Western Europe. New evidence from an extremely precisely ^{14}C dated loess sequence in Hungary points to a close link between abrupt climate change and dust dynamics in Central Europe (Újvári et al., 2017), while increasing evidence points to pervasive millennial scale cyclicity in ice rafted

debris originating from the BIIS (Scourse et al., 2009; Haapaniemi et al., 2010). A number of other climate records in Central and Western Europe also suggest a highly dynamic last glacial climate, but many European loess records lack sufficiently detailed independent age control and in the British Isles there is a lack of detailed, continuous climate archives for this interval that would shed light on climatic variability over westernmost Europe.

In summary, while loess accumulation in southern Britain, last glacial climate change, BIIS and FIS dynamics, and North Sea drainage, are all likely to be closely linked, the timing of loess accumulation with respect to ice sheet dynamics and last glacial climate change remains untested. The uncertainties above can be addressed through detailed dating and analysis of loess deposits in SE England. An ideal candidate is the loess section at Pegwell Bay, eastern Kent (Fig. 1), Britain's most studied loess section. Here we undertake a detailed luminescence and environmental proxy analysis of the Pegwell Bay section with the aim to understand dust accumulation dynamics and climate under the loess depositional period, and its causal relationship to prevailing ice sheet and atmospheric conditions over NW Europe.

2. Pegwell Bay: Britain's most studied loess site

2.1. Site background

The Pegwell Bay loess sequence crops out at the extreme eastern edge of the Isle of Thanet (eastern Kent) and is exposed at the sea cliffs of Pegwell Bay (Fig. 1). The up to 4 m thick sequence unconformably overlies the late Palaeocene marine sands of the Thanet Formation or heavily brecciated upper Cretaceous chalk (Pitcher et al., 1954). Extensive solifluction and cryogenic features in underlying rocks and sediments point to permafrost conditions prior to loess accumulation (Murton et al., 2003). The loess attains its thickest expression over the Thanet Formation at Cliffs End (Fig. 1), the site of a former hover port.

First studied by Pitcher et al. (1954) and Kerney (1965), the stratigraphic sequence shows a number of striking features (Fig. 2 and Appendix A Fig. S1). The loess sequence is capped by a grey to brown modern/Holocene soil, below which lies a non-calcareous blocky brownish loess. Underlying this, an abrupt boundary marks the transition to a calcareous yellow loess with faint brown banding in the upper part and sandy bands towards the base. Also of note is a distinct band of scattered, vertical or high angle inclined black flint pebbles in the lower 30 cm of the calcareous loess that point to frost heaving operating early in loess deposition (Pitcher et al., 1954). The interpretation of many of these stratigraphic features is still debated, particularly the cause of the sharply distinct calcareous and non-calcareous loess units, which has been variously tied to changes in loess sources, an unconformity, and soil formation (Pitcher et al., 1954; Kerney, 1965; Catt, 1977; Clarke et al., 2007). A number of fundamental questions are therefore still outstanding regarding the loess at Pegwell Bay: notably the start and end date for dust deposition, whether there were multiple phases of deposition or reworking, if an unconformity exists, or whether soil formation acting on a single loess unit alone explains the site stratigraphy. Without answers to these questions, the significance of the site for understanding dust and climate history for NW Europe during the last glacial remains uncertain.

2.2. Site stratigraphy

The sampled section described here (Fig. 2) is c. 3.5 m thick, with the upper c. 3.3 m of the exposure comprising loess or soil formed on loess (enlarged stratigraphic log is shown in Appendix A Fig. S1). The lighter, sandy Thanet Formation at the base is overlain by open, porous, buff coloured calcareous loess with faint carbonate flecks and few carbonate-lined root traces. At the bottom, the loess is sandier and shows iron staining, while from 3.15 to 3.35 m it contains upturned, rounded black flint pebbles, as first described by Pitcher et al. (1954). From c. 2.7–2.9 m from the top, a sequence of fine sandy bands of c. 0.5–1 cm thickness alternating with darker (siltier?) bands is exposed. Additionally, at around 1.9–2.1 m a series of faint but darker bands (reminiscent of the overlying non-calcareous loess) is exposed without any clear change in particle

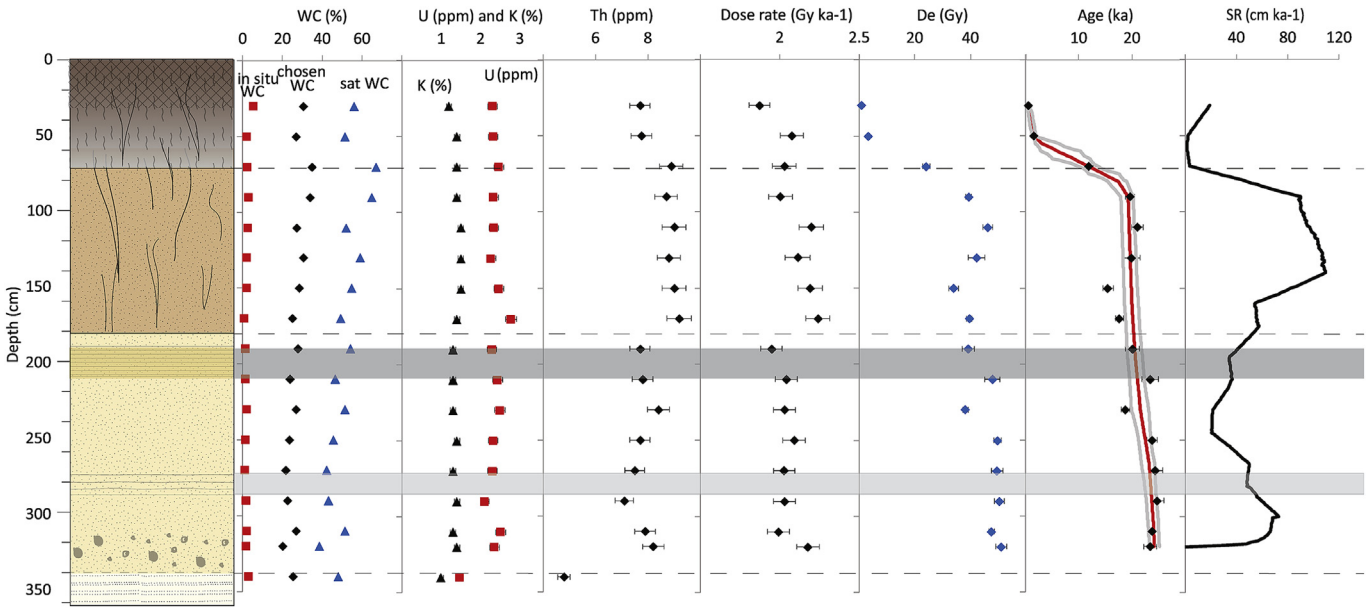

Fig. 2. Luminescence dating results alongside site stratigraphy (see Fig. S1). WC = water content and SR = sedimentation rate. Luminescence ages are presented alongside the results from the age-depth model for the section (see section 3.1). The red line is the median fit while the grey lines represent 95% confidence ranges on the ages. Error bars on dose rate, De and age are all 1σ. Stratigraphic boundaries are marked by dashed lines while the sandy unit and darker unit in the calcareous loess are marked by light and dark grey bands respectively. (For interpretation of the references to colour in this figure legend, the reader is referred to the Web version of this article.)

size. This lower loess continues up to c. 1.78 m where a sharp boundary occurs with the overlying non-calcareous loess. The overlying loess is darker in colour but apparently still porous and with fine root traces. In contrast to the loess below, there are abundant root channels infilled with darker overlying material in this unit. Upwards in the unit, the loess becomes darker, blockier in structure, and with few sporadic gravel particles in the top c. 1 m. At c. 0.45 m there is a noticeable change to darker and more orange colour and at this point there are abundant root traces, infilled root systems and occasional stones and pebbles. The top 0.25 m comprises a dark brown to grey organic rich top soil with abundant modern roots and scattered angular flint gravels.

3. Methods

In order to address the aims outlined in section 1, we adopt a high sampling resolution luminescence dating approach and multi–proxy analysis combining mineral magnetic, particle size and geochemical analyses, to understand sedimentation, soil formation and palaeoenvironment. Fieldwork took place in early March 2019, where the S-SE facing cliff section exposing c. 3.2 m of loess at the former hover port site (Figs. 1 and 2 and figure S1; N51° 19.651′, E001° 22.200′; TR 3464 8811) was sampled every 20 cm for luminescence dating and every 10 cm for grain-size, mineral magnetics and geochemistry.

3.1. Luminescence dating, age modelling and dust accumulation rate

Samples were obtained by hammering c. 10–20 cm long, 4 cm diameter steel tubes into the cleaned exposure. Water contents and dose rates were obtained from sediment from the resulting holes after tube extraction. Samples were processed for luminescence dating in the Laboratory for Luminescence Dating at the University of Sassari, Sardinia, Italy. Sample tubes were opened under subdued red light. The outer 5 cm parts of sediment were scraped off and, the inner material not exposed to the light was used for luminescence dating. Sediment was treated with 40% HCl and 30% H_2O_2 to remove carbonate and organic matter respectively, and then wet sieved at different grain-sizes. The grain-size fraction 60–90 μm was chosen for De measurement and pure quartz separates from this fraction were extracted by two step heavy liquid separation with sodium polytungstate (2.70 g cm^{-3}; 2.62 g cm^{-3}). Finally, quartz grains were soaked in 40% HF for at least for 1 h to remove remaining K-feldspar grains and etch the quartz α-irradiated rims (Porat et al., 2015). All luminescence analyses were carried out using a Risø TL/OSL-DA-20 reader equipped with calibrated 90Sr/90Y beta sources (of ~0.114 Gy s^{-1}). Multi-grain small aliquots (approximately 200 grains) were mounted on stainless steel discs of 0.9 mm in diameter and 0.2 mm in thickness using silicone spray (Duller, 2008). These quartz aliquots were stimulated using blue light emitting diodes (LED) (λ ¼ 470; FWHM 20 nm; w80 mW cm^2) and the resulting Optically Stimulated Luminescence (OSL) signal was detected throughout a 7.5 mm UV glass filter (Hoya U-340; 280–380 nm). A modified single aliquot regenerative-dose (SAR) protocol was used to determine the quartz OSL equivalent doses (De) (Murray and Wintle, 2000, 2003). The fast component of net quartz OSL was isolated using the first 0.8 s of signal with the following 0.8–2 s subtracted as background (Cunningham and Wallinga, 2010). The specific settings and performance of the SAR protocol and estimated De reliability are reported below in sections 4.1 and 4.2. At least 24 aliquots for each sample were analysed for De determination. The performance of protocols and quality of measurements were monitored through dose recovery tests and standard aliquot rejection criteria: i) recycling ratio (ratio between two identical regeneration points), ii) recuperation (signal from a zero dose regeneration point) and iii) natural signal < 3σ above background (Wintle and Murray, 2006). The sensitivity corrected dose response curve for each signal was fitted using a single exponential function (to obtain the saturation value of $2D_0$ of the natural De). Only those aliquots that were capable of measuring the dose of interest (i.e. with sufficiently large D_0) were considered for De calculation while those with $2D_0$<De (De average of all aliquots) were considered saturated and thus rejected and not included in the De calculation (Yi et al., 2016; Thomsen et al., 2016).

For water content measurements (expressed as fraction of sample weight in %), ~140 g of each sample was weighed and then left in the oven at 50 °C for two days. Following this drying, the samples were weighed again to measure the loss of water and thus the in situ field water content was calculated (initial weight - dry weight/dry weight). Water was then added until plastic limit behaviour was achieved (saturation limit). After 24 h the saturated weight was measured to obtain saturation water content (sat weight-dry weight/dry weight). In situ water contents were certainly affected by drying at the exposure (which is southeast facing). However, although the climate in the study area is relatively cool and moist, due to loess porosity and the underlying sandy Thanet Formation, it seems unlikely that the loess was completely saturated since burial (although it is likely there were phases of saturation). To account for inter sample variation due to grain size and composition, we therefore take the average of the in situ and saturated water contents measured as above as the closest approximation of burial conditions. These values (outlined in the section 4.2) are close to typical loess values in moist areas, although to account for the necessarily high uncertainty on these assigned estimates of geologic water content we incorporate an error uncertainty of 20%.

Dose rates were obtained on a per sample basis through measurement of U, Th and K concentrations after milling and via sodium peroxide fusion ICP-MS at SGS Minerals, Canada. The radionuclide concentrations were converted to dry dose rates using the conversion factors provided by Guérin et al. (2011). An internal dose rate from U and Th of 0.02 ± 0.01 Gy ka^{-1} was assumed based on Vandenberghe et al. (2008). The contribution of cosmic rays to the total dose rate was calculated according to Prescott and Hutton (1994).

In order to obtain a continuous age-depth model from the luminescence ages, a Bayesian modelling approach using the Bacon code of Blaauw and Christen (2011) was undertaken at 1 cm depth resolution, an approach successfully applied to Chinese and Serbian loess (Stevens et al., 2018; Peric et al., 2019). Bacon uses Bayesian statistics to reconstruct accumulation histories for deposits, through combining numerical age dates with prior information such as accumulation rate and its variability (memory). Accumulation rates are controlled using a gamma autoregressive semi-parametric model with an arbitrary number of subdivisions along the sediment profile (Blaauw and Christen, 2011). Prior knowledge about accumulation rates can lead to reduced uncertainty and more realistic modelling (Blaauw and Christen, 2011). The priors for accumulation rate and memory (autocorrelation) are modelled by gamma and beta distributions, and the latter defines how much the accumulation rate at a particular depth depends on the accumulation rate of the neighbouring depths. The section thickness dictates to some degree the flexibility of the age-depth model, which is obtained by millions of Markov Chain Monte Carlo (MCMC) iterations (Blaauw and Christen, 2011). Outlier ages and their errors are modelled using student-t distributions. In this way, age inversions, age uncertainties, and scatter in the age data are accounted for to

create the most realistic age-depth model for a stratigraphic sequence, based on input ages. All systematic errors were removed prior to age modelling. Output from the modelling defines the age-depth model, which was then used to derive sedimentation rates. The latter were obtained at arbitrary 1 cm intervals based on changing depth with age in the model output, and then smoothed via calculation of a running 20 cm mean, in order to remove fine-scale sedimentation rate variability that greatly exceeds the uncertainty of the age-depth model. In order that the results can be reliably compared between regions and other dust archives, as well as for use in estimating past atmospheric dust flux (Albani et al., 2015), we here also calculate dust Mass Accumulation Rate (MAR) (Kohfeld and Harrison, 2003). Dust MAR (g m^{-2} a^{-1}) is calculated using the following equation:

$$MAR = SR \times f_{eol} \times BD,$$

where SR is sedimentation rate (m a^{-1}), f_{eol} is the proportion of the sediment that is aeolian (assumed = 1), and BD is bulk density of the loess (g cm^{-3}). Bulk density values for Pegwell Bay loess were not measured directly but estimated bulk density for typical loess values from Europe and China tend to average around 1.5 g cm^{-3} (Buylaert et al., 2015; Kohfeld and Harrison, 2003; Peric et al., 2019; Stevens et al., 2016; Újvári et al., 2010).

3.2. Rock magnetic experiments

After drying and weighing, mass corrected magnetic susceptibility was measured on all samples using an Agico Kappabridge MFK1-FA at Uppsala University. The MFK1-FA is the most sensitive commercially available instrument for measuring bulk magnetic susceptibility in weak magnetic fields. Each sample was measured three times at 976 Hz (χlf) and 15,616 Hz (χhf) (Hrouda, 2011) in a peak field of 200 A m^{-1}, and the mean values of the three measurements were used to calculate mass dependent susceptibility in m^3 kg^{-1}. A reference sample with known magnetic susceptibility was also measured at both frequencies to check instrument drift during measurement. χlf measures the total ferri- and ferromagnetic assemblage, while χhf excludes the finer grained (0 to c. 0.03 μm diameter) superparamagnetic (SP) grains (Dearing et al., 1996). The frequency dependence of magnetic susceptibility can therefore yield information about the influence of fine-grained SP grains on the magnetic susceptibility signal, and in many instances is used as an indicator of soil formation (Maher and Taylor, 1988). Frequency dependence as a percentage χfd (%) was calculated by the following relationship:

$$\chi fd\ (\%) = ((\chi lf - \chi hf) / \chi lf) \times 100,$$

while frequency dependence as the difference between χlf and χhf (Δχ) is simply:

$$\Delta\chi\left(m^3 kg^{-1}\right) = \chi lf - \chi hf.$$

To further investigate how the magnetic susceptibility signal varies with frequency, three samples (one from the upper soil and one each from the two loess units) were measured on an Acrea DynoMag system at Uppsala University, at frequencies ranging from 5 to 100,000 Hz. As this is the first detailed mineral magnetic analysis of loess in southern Britain, for comparison, a Lower Pleistocene loess sample from the Lantian section on the Chinese Loess Plateau was also measured. Chinese loess is well understood in terms of the enhancement of the magnetic susceptibility signal (pedogenic model) and so provides a useful comparison point for the new data from Pegwell Bay.

Rock magnetic experiments were performed at the Paleomagnetic Laboratory of the University of Burgos (Burgos, Spain). To estimate the domain state of the ferromagnetic (s.l.) minerals, hysteresis measurements and stepwise isothermal remanent magnetization (IRM) acquisition experiments were conducted on a Variable Field Translation Balance (MMVFTB, Magnetic Instruments). A maximum applied field of 1T (the limit of the instrument) was used during the IRM, hysteresis and backfield coercivity measurements. IRMs were measured in ~25 steps. The S300 proxy was determined from the backfield curve, obtained during the hysteresis experiments by RockMagAnalyzer 1.0 software (Leonhardt, 2006; Bloemendal et al., 1992). This can be used to examine the relative amounts of higher (hematite, goethite) and lower (magnetite, maghemite) coercivity magnetic contributors, with lower S300 values indicating increasing amounts of higher coercivity minerals.

The coercivity of remanence (remanent coercive force) to coercivity ratio (Hcr/Hc) and saturation remanence to saturation magnetization ratio (Mrs/Ms) allow so-called Day plot analysis (Day et al., 1977; Dunlop, 2002). This was used to reveal the multidomain, single-domain (SD), superparamagnetic (SP) and pseudo-single domain (PSD) state (in later studies: SD + MD mixture; Dunlop, 2002; or vortex state (VS); Roberts et al., 2017) of the magnetic mineral components in the samples. The Day plot is a commonly applied method in the study of the grain size of magnetic contributors in loess (e.g. Liu et al., 1992; Lagroix and Banerjee, 2002; Pan et al., 2002; Taylor et al., 2014; Necula et al., 2015).

Thermomagnetic experiments (temperature dependence of the magnetization) were also executed by MMVFTB from room temperature (~20–25 °C) up to 700 °C in air. Temperature variation in magnetization provides information about the transformation and, e.g., the Curie temperature (Tc) of magnetic mineral components, by the change in magnetic moment at different temperatures during heating and cooling. The dia/paramagnetic correction of the hysteresis data, determination of Curie temperature (from second derivative and following the way of Moskowitz (1981)), and the results of rock magnetic measurements, were obtained by RockMagAnalyzer1.1 software (Leonhardt, 2006).

Along with various magnetic contributors, loess contains unstable maghemite, revealed by a bump on the heating curve around 250 °C, the mark of its decomposition (Gao et al., 2019). Maghemite seems to be a common contributor in loess-palaeosol successions (e.g., Evans and Heller, 1994; Liu et al., 2010; Deng et al., 2000; 2001; Zhu et al., 2001; Bradák et al., 2018; Gao et al., 2019). Unstable maghemite can form by chemical alteration, which makes it a sensitive environmental proxy. The characteristic change on thermomagnetic curves at around 250 °C was therefore used to determine the relative maghemite content of the samples and create a maghemite content proxy. After recognizing the "maghemite feature" on the thermomagnetic heating curve, the first derivative of the data was used to clearly identify the section of the curve representing the maghemite alteration. The first derivative curve was used to calculate the relative change in magnetization as a representative feature for the amount of transforming maghemite (i.e., the relative maghemite content of the sample). Application of a linear trend line on the section representing the maghemite alteration helped to calculate the noise that may influence analysis of the results. The deviation of the data points from the trend shows this noise, and therefore the maximum distance of data points above and below the trend line was used to quantify this.

Anhisteretic remanent magnetization (ARM) was acquired in a peak of 20, 30 and 60 mT and a steady field of 0.1 mT, and measured using a 2G Enterprises Superconductor Cryogenic Magnetometer

2G-755, with automatic system of AF demagnetization and ARM indicator. ARM susceptibility (χARM) was then calculated. In general, ARM is sensitive to the concentration of finer grain (<10 μm) magnetite (Opdyke and Channell, 1996) and χARM can therefore be used as a proxy of fine grain (SD and PSD) soft magnetic contributors (King et al., 1982).

3.3. Grain size

Samples for grain-size analysis were first oven dried at 50 °C for 24 h and delicately homogenized to break down larger aggregates. Sub samples of c. 3 g were then treated with 12% HCl to remove carbonates and 33% H_2O_2 to remove organic matter. Samples were then immersed in 0.5% $(NaPO_3)_6$ and ultrasonicated briefly prior to analysis. Grain-size distributions were measured by three repeat measurements on a Malvern Mastersizer X at Uppsala University with a He–Ne laser (λ = 632.8 nm) under the polydispersive model and using a 300 mm lens capable of detection of 1.2–600 μm particles. The average distributions were then used in further analyses after exclusion of obvious outliers. Although complicated by factors such as source distance and sediment availability (Újvári et al., 2016), grain-size distribution shape can help determine loess transport and depositional processes (Vandenberghe, 2013). In addition to distribution statistics and % of different grain size classes, the U-ratio was also calculated (Vandenberghe and Nugteren, 2001). The U-ratio is the ratio of the % 16–44 μm fraction to the % 5.5–16 μm fraction and is designed to exclude grains formed during in situ weathering and grains brought in by local saltation. Arguably then, the U-ratio is a better indicator of the intensity of wider-scale aeolian activity, with higher values denoting stronger winds or a more dynamic aeolian environment.

3.4. Elemental geochemistry

Elemental/oxide chemistry of the loess at Pegwell Bay was determined by X-ray fluorescence spectroscopy (XRF). Samples were first oven dried at 50 °C for 12 h minimum and then pulverised to a powder using a quartz mill. Ground samples were then packed into Bruker measuring containers covered with prolene film prior to measurement on a Bruker TRACER 5i used in fixed laboratory position at Uppsala University. In-built GeoMining and GeoExploration calibrations were used to obtain the majority of element/oxide concentrations, empirically corrected for known offsets obtained from known concentration samples. NaO, MgO and Al_2O_3 are unmeasurable or do not perform well with the in-built Tracer calibrations, and as such a specific calibration was created for these oxides using Bruker EasyCal software and a group of known concentration samples after measurement via sodium peroxide ICP-MS and wavelength dispersive XRF at SGS Minerals Canada. Under this calibration, samples were measured in a He atmosphere with no filter window. Each sample was measured three times and the average used for further analysis. All abundant elements are presented as oxides irrespective of machine output and these major oxides were summed and normalised to 100%. The oxide concentrations used for calculation of weathering indices (below) were calculated according to their molar masses. Sample geochemistry provides insight into weathering, source change and grain-size change. In addition to presenting concentrations and ratios of key elements as weathering indicators, key weathering indices were also calculated. Firstly, the Chemical Index of Alteration (CIA) (Nesbitt and Young, 1982) was used to yield a quantitative measure of feldspar weathering. In the case of weathering intense enough to alter K-feldspar and plagioclase, the mobile elements Na, Ca and K should all be removed, leading to enrichment of immobile element Al (Buggle et al., 2011). A higher value on the index therefore indicates higher rates of weathering, as defined in the equation below:

$$CIA = (mAl_2O_3 / (mAL_2O_3 + mCaO* + mNa_2O + mK_2O)) \times 100,$$

where *m* denotes molar mass and CaO* is the assumed CaO content from silicate minerals, in order to remove the influence of CaO from carbonates and phosphates. If the CaO value is lower or equal to Na_2O then the former value is used, while if CaO is higher than the Na_2O content then the Na_2O value is used instead. However, as the Pegwell Bay sequence will be dominated by the major change from calcareous to non-calcareous loess, major oxide abundances also were recalculated after removing CaO and renormalizing. A Ca-free weathering index (the Chemical Proxy of Alteration (CPA)) was then calculated (based on Cullers, 2000):

$$CPA = (mAl_2O_3 / (mAl_2O_3 + mNa_2O)) \times 100.$$

This index also removes the influence of K_2O, which can be advantageous due to inconsistent K behaviour during weathering (Buggle et al., 2011).

4. Results

4.1. Luminescence tests

Detail of the luminescence tests are provided in Appendix A, while a summary is presented here. The purity of quartz material was monitored using the OSL IR-depletion ratio test (Duller 2003). All samples showed an OSL depletion ratio within 10% of unity, indicating null or insignificant IR-sensitive feldspar contributions to the net OSL decay signal (Duller 2003). In order to select the appropriate thermal treatment for the SAR protocol, the De and dose recovery ratio dependency on temperature were monitored through pre-heat plateau tests and temperature dependent dose recovery tests respectively, while the effect of thermal transfer on samples was also monitored (Fig. S2). On the basis of these experiments, we set the SAR protocol with a preheat of 220 °C (duration: 10s) and a cut heat of 180 °C for De measurements for all samples. Each SAR cycle was finished with a high temperature (280 °C) blue light stimulation for 40 s. Example sensitivity corrected dose response curves and the OSL signal decay curves are shown in Fig. S3 and are dominated by the fast component, exhibiting good performance of recycling ratio and recuperation. However, sample PB340, taken at the boundary with the Thanet Formation, is completely beyond the saturation limit. To test for reproducibility of the chosen protocol a series of dose recovery tests were carried out for five samples down the section (Fig. S3). Our SAR protocol performs well and exhibits good internal reproducibility among samples. It is able to measure a quartz dose given prior to heat treatment with an acceptable degree of accuracy.

4.2. Luminescence dating

The outcome of the luminescence dating is shown in Table 1 and Fig. 2. De values were calculated via weighted means (Sechi et al., 2020). Abanico plots showing De distributions as well as statistics are given in Fig. S4 and Table S1 respectively, while Appendix A outlines the rationale for De calculation. Age versus depth is shown in more detail in Appendix A Fig. S5. Quartz OSL De values and ages generally show small decreases with decreased depth up to 70 cm in the section, the approximate boundary with the upper soil unit. Above that there is a rapid decrease in values in the top 50 cm. Some reversals in age and De are visible, especially between

Table 1
Luminescence dating results for all samples. WC = water content (±20%). Water content was chosen based on the average of the in situ and saturation value for individual samples. For samples PB50, PB230 and PB320 no water contents are available and the average for the whole PB section was used. DR = dose rate and n = number of aliquots analysed. OD = overdispersion. All radioisotopes are presented with ±5% uncertainty. Cosmic dose rate is calculated based on Prescott and Hutton (1994). Uncertainty on ages contains both random and systematic components. Sat. = saturated and no De/age calculated.

Sample	Depth	WC	U	Th	K (%)	Cosmic DR	Total DR	De (Gy)	n	OD	Age (ka)
	(cm)	(%)	(ppm)	(ppm)		(Gy ka^{-1})	(Gy ka^{-1})	(%)			
PB30	30	31	2.3 ± 0.1	7.7 ± 0.4	1.2 ± 0.1	0.19 ± 0.01	1.87 ± 0.06	1.0 ± 0.1	19	22	0.5 ± 0.0
PB50	50	27	2.3 ± 0.1	7.8 ± 0.4	1.4 ± 0.1	0.18 ± 0.01	2.08 ± 0.07	3.3 ± 0.2	12	30	1.6 ± 0.1
PB70	70	35	2.5 ± 0.1	8.9 ± 0.4	1.4 ± 0.1	0.18 ± 0.01	2.03 ± 0.07	24.1 ± 1.4	22	35	11.9 ± 0.8
PB90	90	34	2.3 ± 0.1	8.7 ± 0.4	1.4 ± 0.1	0.17 ± 0.01	2.00 ± 0.07	39.4 ± 0.9	20	22	19.7 ± 0.9
PB110	110	27	2.3 ± 0.1	9.0 ± 0.5	1.5 ± 0.1	0.17 ± 0.01	2.20 ± 0.08	46.3 ± 1.7	9	17	21.0 ± 1.1
PB130	130	31	2.3 ± 0.1	8.8 ± 0.4	1.5 ± 0.1	0.16 ± 0.01	2.11 ± 0.11	42.2 ± 2.9	24	39	20.0 ± 1.6
PB150	150	29	2.5 ± 0.1	9.0 ± 0.5	1.5 ± 0.1	0.16 ± 0.01	2.19 ± 0.08	34.0 ± 1.8	22	30	15.5 ± 1.0
PB170	170	25	2.8 ± 0.1	9.2 ± 0.5	1.4 ± 0.1	0.16 ± 0.01	2.24 ± 0.07	39.6 ± 1.0	18	12	17.7 ± 0.7
PB190	190	28	2.3 ± 0.1	7.7 ± 0.4	1.3 ± 0.1	0.15 ± 0.01	1.95 ± 0.07	39.2 ± 2.2	18	21	20.1 ± 1.3
PB210	210	24	2.4 ± 0.1	7.8 ± 0.4	1.3 ± 0.1	0.15 ± 0.01	2.04 ± 0.07	47.9 ± 2.7	20	15	23.5 ± 1.5
PB230	230	27	2.5 ± 0.1	8.4 ± 0.4	1.3 ± 0.1	0.14 ± 0.01	2.03 ± 0.07	38.1 ± 1.0	24	13	18.8 ± 0.8
PB250	250	24	2.3 ± 0.1	7.7 ± 0.4	1.4 ± 0.1	0.14 ± 0.01	2.09 ± 0.07	49.7 ± 1.3	35	10	23.8 ± 1.0
PB270	270	22	2.3 ± 0.1	7.5 ± 0.4	1.3 ± 0.1	0.14 ± 0.01	2.03 ± 0.07	49.6 ± 2.0	15	11	24.5 ± 1.3
PB290	290	22	2.1 ± 0.1	7.1 ± 0.4	1.4 ± 0.1	0.13 ± 0.01	2.03 ± 0.07	50.3 ± 1.8	21	13	24.8 ± 1.2
PB310	310	27	2.5 ± 0.1	7.9 ± 0.4	1.3 ± 0.1	0.13 ± 0.01	1.99 ± 0.07	47.6 ± 0.9	19	12	23.9 ± 1.0
PB320	320	20	2.4 ± 0.1	8.2 ± 0.4	1.4 ± 0.1	0.13 ± 0.01	2.18 ± 0.07	51.1 ± 0.9	15	15	23.5 ± 1.2
PB340	340	25	1.5 ± 0.1	4.8 ± 0.2	1.0 ± 0.1	0.13 ± 0.01	1.43 ± 0.05	Sat.	–	–	–

230 and 150 cm. De values show similar depth patterns to the ages. Dose rate shows a marked increase in the upper non-calcareous loess unit, driven largely by increases in Th and U content. Water contents show gradual decreases with depth with no major change between the two loess units. There appears to be no substantial change in age across the stratigraphic boundary between the two loess units.

4.3. Age modelling and MAR

To the best of our knowledge, these data comprise the most stratigraphically detailed age analysis of any English loess deposit, and represent a unique opportunity to investigate climate, dust activity and loess depositional dynamics at the margin of the European loess belt very close to the North Atlantic. However, we must first develop an age model based entirely on the OSL ages, through which dust MARs can be calculated and climate proxies plotted on entirely independent age axes. Approaches to construct age models from OSL datasets vary considerably (e.g., Stevens et al., 2008; 2016; Sun et al., 2011; Kang et al., 2015; Lu et al., 2013; Peric et al., 2019); but here we apply the Bacon code-based Bayesian age model of Blaauw and Christen (2011). Due to the abrupt change in ages at the base of the upper soil, two separate age model runs were initiated and joined together in order to select different priors for the two parts of the sequence. For the lower part to 80 cm default priors were used except 'thick', which was set to 35 to avoid the model following ages too closely due to the age inversions in the middle of the sequence. For the upper 80 cm 'acc.mean' was set to 35 and 'mem.strength' to 2 to reflect the lower accumulation rate. The results of the age modelling are shown in Fig. 2, and data presented in Appendix B. Derived sedimentation rates are also shown in Fig. 2, while dust MAR values for the main period of loess deposition are shown by age model age in Fig. 3. Dust MAR data is also presented in Appendix B. There is considerable variability in resultant apparent sedimentation rate and dust MAR. The peaks in accumulation occur broadly at c. 25–23.5 ka and c. 20–19 ka (Fig. 3). At these ages, the 95% confidence ranges imply an uncertainty of around ±1 ka on these peaks. We note that derivation of sediment accumulation rates from age depths models comes with substantial uncertainty (Trachsel and Telford, 2017). However, although exact values of dust MAR should be considered only as approximate, the presence and timing of these peaks should be accurately described and this approach represents the currently best available method for deriving age depth relationships. The two main peaks of accumulation do not exactly coincide with the two loess units, although the first peak occurs entirely in the lower part of the calcareous unit. It should also be noted that the relative magnitude of these two accumulation peaks is strongly affected by the scatter in ages at 150 and 230 cm, and should only be taken as a rough indication. Above the soil horizon at 70 cm it should also be kept in mind that soil formation will likely have affected the OSL ages, and this makes calculation of a depositional age model and derivation of accumulation rates in the upper 70 cm problematic. This is discussed further in section 5.2. Irrespective, the luminescence-based age model shows two greatly enhanced phases of loess accumulation during the late last glacial, separated by a phase of lower accumulation rate around 23–21 ka.

4.4. Mineral magnetics

Low frequency magnetic susceptibility (χlf) and frequency dependence (χfd and $\Delta\chi$) show generally lower values in the lower loess unit, with gradually increasing values from the boundary between the two loess units (Fig. 4). Xlf peaks just below the upper soil unit, while χfd peaks further up in the soil. There is little finer scale variability in the proxies but small reductions in χlf occur within the Thanet Formation, the sandy unit around 280 cm, and the darker banded unit at around 200 cm χlf values are relatively low (c. 1–3x10^{-7} m^3 kg^{-1}) while χfd is around 4–6% in the loess, and increases to c. 10% in the upper soil. Fig. S6 shows more detailed mineral magnetic analyses, outlined in the online Appendix. In sum, similar trends are shown in for magnetic susceptibility but the coercivity of the remanence to coercivity ratio (Hcr/Hc) shows very slightly lower ratios in the non-calcareous loess unit and χARM is more variable in the loess units and exhibits a more defined peak at the base of the upper soil (40–60 cm).

To investigate the enhancement of the magnetic susceptibility signal in more detail, χlf was plotted against $\Delta\chi$ for the Pegwell Bay samples (Fig. 5A) along with data from the Romanian middle to late Quaternary loess-palaeosol section at Semlac (Zeeden et al., 2016). In our plot the data have been normalised by frequency (χfn) to allow comparison between data obtained under different

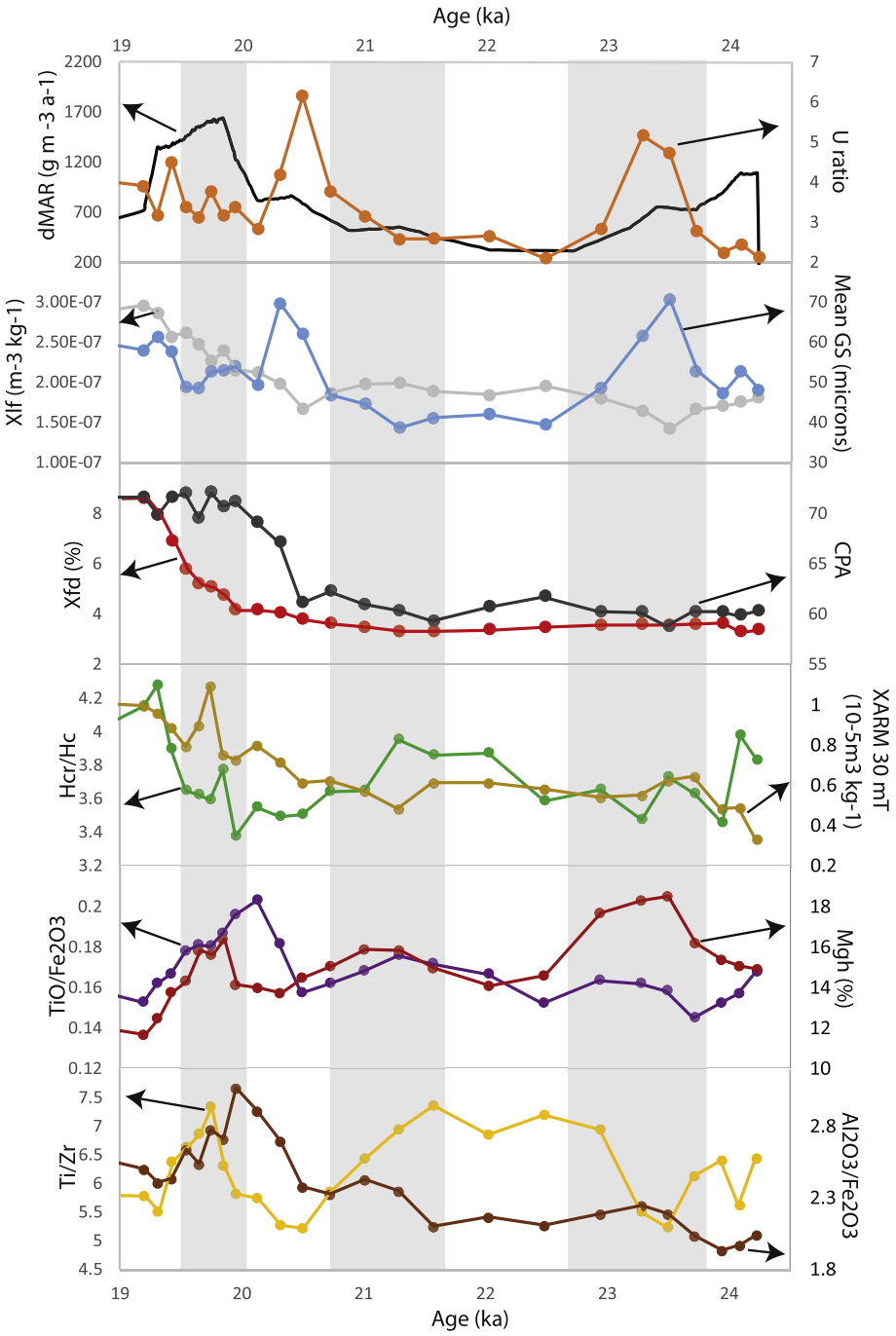

Fig. 3. Dust (d) MAR and key climate/environmental proxies plotted by age model age during the main period of loess deposition at Pegwell Bay. Proxy records are described in Fig. 4, Appendix A and manuscript text. The three grey shaded bands indicate phases of increased maghemite (Mgh) %.

instruments and frequency settings (Hrouda, 2011). This approach was proposed by Zeeden et al. (2016; 2018) based on Forste et al. (1994) to allow analysis of the mode of susceptibility signal acquisition. Note that the 'true loess line' in Fig. 5A represents the expected trend in the data if the pedogenetic enhancement model of loess susceptibility applies to the data (as is the case at Semlac; Zeeden et al. (2016)), while deviations from that line may suggest other models of signal enhancement and depletion. The Pegwell Bay data generally plot to the left of the true loess line, although values from the upper soil overlap the line. Data from the lower loess unit plot a steeper trend to the true loess line, while data from the upper loess unit plot a shallower trend (i.e., greater increases in $\Delta\chi$ compared to χlf (Fig. 5A)). To further explore the change in susceptibility with frequency, the magnetic susceptibility of three selected samples from the soil (PB60), non-calcareous loess (PB140) and the lower calcareous loess (PB260) was measured at multiple frequencies alongside an early Quaternary loess sample from Lantian, on the well understood Chinese Loess Plateau (Fig. 5B). The results clearly show the relatively low susceptibility values in the Pegwell Bay material, and point to differing trends in susceptibility loss with increasing frequency. While the Chinese loess sample shows steady decreases in susceptibility with frequency increase,

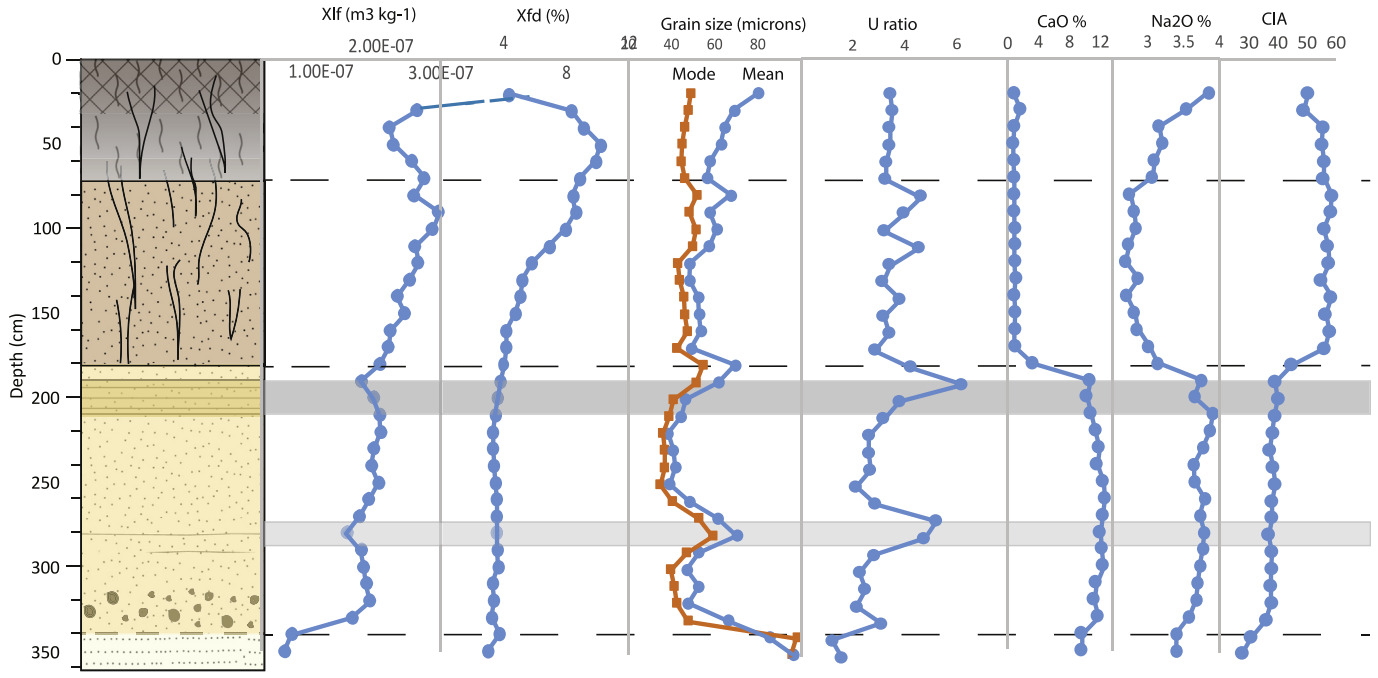

Fig. 4. Key proxies by depth at the Pegwell Bay section alongside stratigraphy (see Fig. S1). Low frequency magnetic susceptibility (χlf m^3 kg^{-1}), frequency dependence (χfd %), mode and mean grain-size (μm), U ratio, CaO (%), Na_2O (%) and Chemical Index of Alteration (CIA). For detailed mineral magnetic, grain-size and geochemical data see Figures S6 to S9.

consistent with signal enhancement via pedogenesis, the Pegwell Bay samples show a more variable trend. This is particularly true for the two loess samples, which show similar behaviour and smaller reductions in susceptibility with increasing frequency, as compared to the Lantian sample, and the soil sample from Pegwell Bay (Fig. 5B). This implies varying and more complex control on magnetic susceptibility signal acquisition in Pegwell Bay loess.

To examine the magnetic mineral grain size of the Pegwell Bay samples, Hcr/Hc was plotted against saturation remanence to saturation magnetization (Mrs/Ms) in a Day-plot (Fig. 5C). Three characteristic groups of samples can be separated in the plot: 1) loess samples defined by Hcr/Hc ~3.5–4.2 (Group 1); 2) some samples from the upper soil and from the upper loess unit characterized by Hcr/Hc ~2.9–3.1 (Group 2); 3) samples from the lowest loess and Thanet Formation boundary with Hcr/Hc ~4.5 and slightly higher Mrs/Ms than the loess and soil samples (Mrs/Ms: ~0.13). Based on the improved Day plot (Dunlop, 2002), the samples fall into the region indicating a mixture of MD and SD grains (PSD region), with c. 20% SD content (Fig. 5C). Magnetization change during heating and cooling can be described by the following characteristics (Fig. 5D). The magnetization changes gradually until ~580 °C. Above ~580 °C a drop of magnetization indicates the Curie temperature (Tc) of magnetite (585 °C). There is still a weak magnetization above the Tc of magnetite, which may relate to oxidised magnetite/maghemite or hematite and fades with increasing temperature around 700 °C. A hump observed at ~250–300 °C may indicate the conversion of thermally unstable maghemite (Gao et al., 2019) (Suppl. Mat.). The maghemite % proxy derived from this observation (See section 3.2) shows four characteristic horizons with increasing relative maghemite content, 40–90 cm, 110–160 cm, 190–230, and 260–300 cm (Fig. S6).

4.5. Grain-size distributions and statistics

Typical grain-size distributions for the upper soil, calcareous and non-calcareous loess units are presented in Fig. 6, which show classic unimodal distributions with silt modes and skews to finer grain-sizes. Generally, the distributions show modal peaks between 40 and 50 μm (Fig. 4) and relatively high sand contents (10–30%; Fig. S7), which also draws up the mean grain-size compared to the mode. Clay content is relatively stable at between 2 and 6%. The U-ratio (Vandenberghe and Nugteren, 2001) indicates shifts in the silt fraction, and follows a similar trend to the mode with depth (Fig. 4). Increased grain-size at the base (340 cm) reflects mixing with the Thanet Formation while substantial peaks occur in grain-size parameters in the banded layer at c. 280 cm, at or just below the boundary between the two loess units, and just below the boundary with the upper soil. The non-calcareous loess unit shows somewhat more variability than the calcareous unit, with the exception of the two peaks at 180–190 cm and 280 cm depth. Grain-size distribution data and statistics are presented alongside dust MAR and age model data in Appendix B.

4.6. Geochemistry and weathering proxies

Variation in CaO and Na2O (%) as well as CIA are shown in Fig. 4. Detailed geochemical data as well as weathering indices and ratios are presented in Fig. S8 and S9 respectively. The most striking feature is the near zero CaO values in the upper soil and loess unit, and the sharp boundary to values around 10–12% in the lower loess unit, more typical for calcareous loess. Sr also changes abruptly at this boundary, likely due to the fact that Sr readily substitutes for Ca (Fig. S8). Other changes across the loess unit boundary are more gradual, with Na_2O showing clear reductions in the upper loess unit. Na_2O also shows increasing values in the upper soil, as does SiO_2 and to some extent MnO. Variations in CIA (Fig. 4) and Rb/Sr (Fig. S9) are strongly affected by the jump in CaO content across the loess unit boundary.

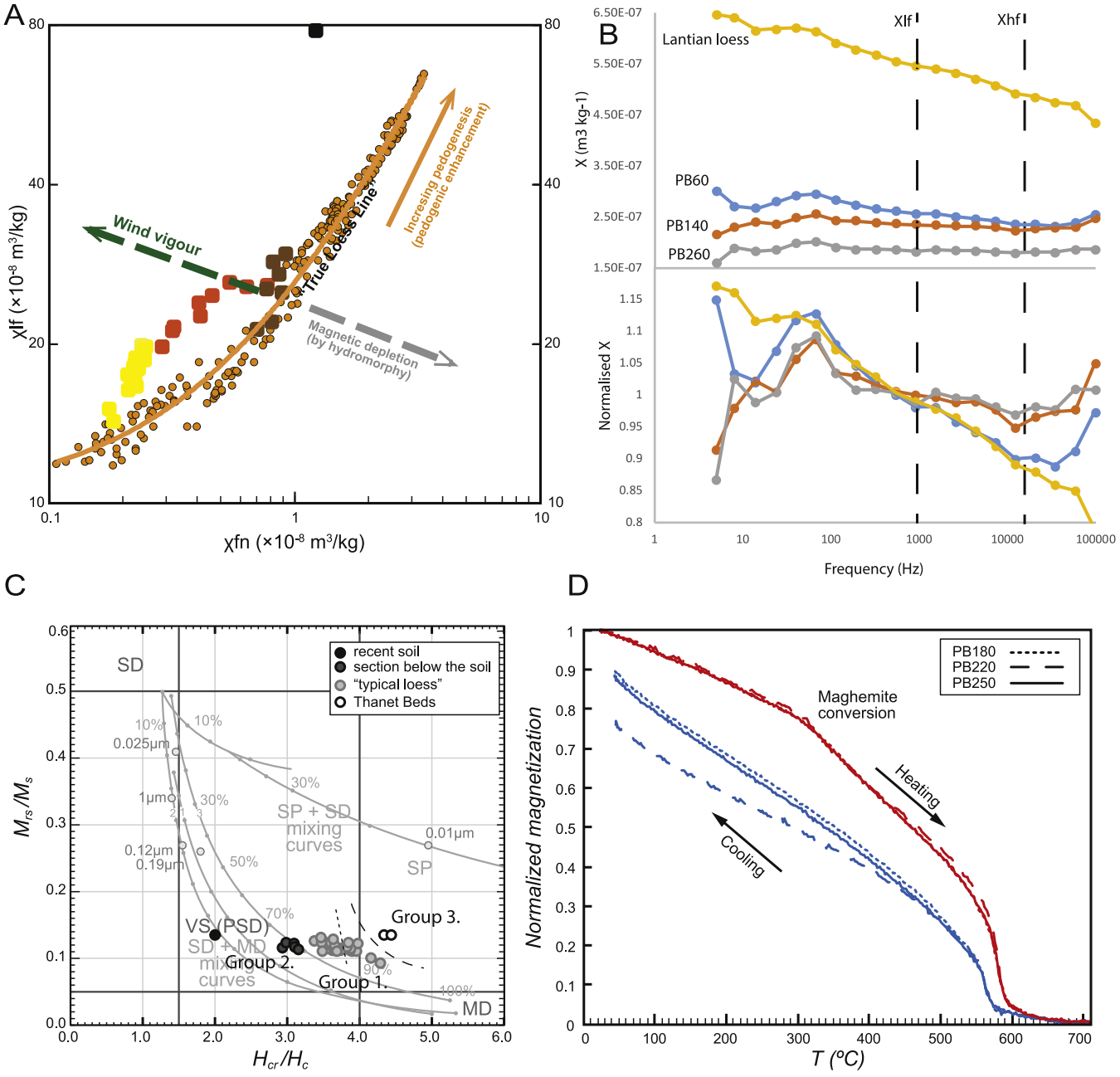

Fig. 5. Rock magnetic investigation of PB samples. A) Xlf versus Δχ normalised to measurement frequency (χfn) showing the pattern of magnetic enhancement in samples from Pegwell Bay (yellow = lower loess unit; red = upper loess unit, brown = upper soil unit) and Semlac, Romania (orange; Zeeden et al., 2016). The orange line marks the best fit line to the Semlac data. According to Zeeden et al. (2016; 2018) the correlation in the Semlac data marked by the 'true loess line' suggests magnetic enhancement caused by climatically controlled loess weathering. The wind vigour and magnetic depletion arrows point to areas on the chart where data would fall if better explained by these alternative models. B) Magnetic susceptibility against measurement frequency for three samples from Pegwell Bay and one sample of Lantian loess. The lower panel shows the data normalised to the average value for ease of comparison. Also shown are the Agico Kappabridge MFK1-FA measurement frequencies used for determining χlf and χhf in all samples in this study (dashed lines). C) Day-plot showing the Mrs/Ms ratio versus the Hcr/Hc ratio for PB samples with sample groups described in the text. Magnetic domain areas (Day et al., 1977) and the mixing curves (Dunlop, 2002). Group 1 = Loess; Group 2 = Upper Soil; Group 3 = Thanet Formation/boundary. D) Example normalised magnetic susceptibility heating and cooling curves (temperature dependent magnetic susceptibility) for three samples. Maghemite conversion may be indicated by the shoulder around 250–300 °C on the heating curve (see section 4.4). (For interpretation of the references to colour in this figure legend, the reader is referred to the Web version of this article.)

5. Discussion

The results above have implications for multiple aspects of understanding the age, formation and alteration of SE English loess, as well as for reconstructing palaeoclimate, dust activity and the influence of ice sheet dynamics on this, over NW Europe. As such, the Discussion below is split up into multiple parts, first dealing with the age of the loess (5.1), and then discussing the inherited characteristics of the loess material and the impact of post depositional alteration (5.2). Subsequently, the cause of the abrupt stratigraphic change between calcareous and non-calcareous loess is discussed (5.3) before an analysis of palaeoclimatic change recorded at the site is presented (5.4). Finally, we present a model of dust mass accumulation rate at the site and for explaining late last glacial

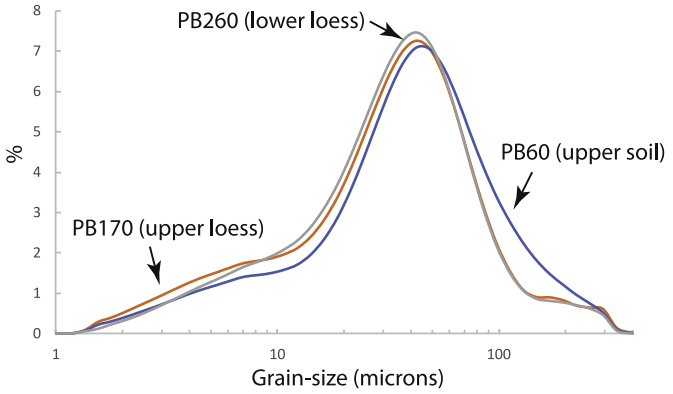

Fig. 6. Example grain-size distributions for the upper soil (blue; PB60), calcareous (grey; PB260) and non-calcareous (orange; PB170) loess. (For interpretation of the references to colour in this figure legend, the reader is referred to the Web version of this article.)

Southern British and NW Europe loess accumulation generally. We link this to ice sheet dynamics, abrupt ice lobe decay and resultant sediment discharge, as well as atmospheric circulation over NW Europe during the late last glacial (5.5).

5.1. Luminescence ages of loess deposition

The luminescence ages presented here (Table, 1; Fig. 2) are older than most previous luminescence age estimates from Pegwell Bay loess, based on TL (14.8 ka, Wintle, 1981; 14.9–18.8 ka, Parks and Rendell, 1992) and post IR OSL (15.0–17.2 ka; Clarke et al., 2007). They are also older than TL ages reported previously for southern England generally (14.5–18.8 ka; Wintle, 1981), and from brickearths from around London (<19 ka; Gibbard et al., 1987). However, more recent TL dating of loess from SE England (Parks and Rendell, 1992) suggested a cluster of ages between 10 and 25 ka, while post-IR OSL ages from stratigraphically similar loess (to Pegwell Bay) from nearby Ospringe yield very similar ages to those presented here (18.7–23.8 ka; Clarke et al., 2007). The ages of loess here are more in line with more recent estimates of the timing of the main last glacial phase of loess deposition in nearby NW France from a variety of sections and using a variety of geochronological methods (Antoine et al., 2016; Guérin et al., 2017).

The quartz OSL signals used here are fast component dominated, show clear reproducibility under the measurement protocol and have passed extensive testing (Figures S2 and 2). It is quite likely that the fading shown in polymineral fine grain OSL and IRSL De values from Ospringe and Pegwell Bay (Clarke et al., 2007) would also have affected age estimates in early polymineral TL work (Wintle, 1981; Gibbard et al., 1987; Parks and Rendell, 1992), meaning these ages may underestimate the true depositional age (Clarke et al., 2007). However, this may not explain the offset from post IR OSL ages from 38 to 53 μm quartz in Clarke et al. (2007). The sampled Pegwell Bay site in Clarke et al. (2007) is both thinner and located further north along the coast. It is hard to compare De and dose rate values in studies where different grain sizes and preparation methods (no etching in Clarke et al. (2007)) were used, but the De values presented here (Table 1) are of the same order as Clarke et al. (2007), while the dose rates here are lower. This is unsurprising given the higher dose rates experienced by un-etched quartz particles (with alpha dose rate) but does not explain the whole age difference. Clarke et al. (2007) used a water content of 10% in their calculations, while here we use closer to 20%, which is more in line with loess studies the world over (Stevens, 2019) and is closer to values used in TL dating of the Holocene soil in the loess at Pegwell Bay by Wintle and Catt (1985). This difference in water content may also account for some difference between the results here and in Clarke et al. (2007) but it is physically not possible to change the water content enough to account for the difference. Recently, Timar-Gabor et al. (2017) have shown that fine-grain quartz ages tend to underestimate the true burial ages at high doses (c. 100 Gy), and compared to other quartz grain sizes. However, this ought not to be a significant factor at the c. 50 Gy doses reported from loess in Kent and in Clarke et al. (2007) the 38–53 μm fraction was used. In Clarke et al. (2007), dose rates were measured using alpha and beta counting and gamma spectrometry, while here ICP-MS was used. Bate et al. (2017) noted a systematic offset in calculated dose rates using gamma spectrometry versus ICP-MS, although not larger than error uncertainty, and Stevens et al. (2007) found ICP-MS and field gamma spectrometry results from Chinese loess produced consistent results. Importantly, it should be noted that there is some variability in luminescence age by depth in the upper non-calcareous loess unit (Fig. 2). In the Clarke et al. (2007) study, only one sample per unit was dated, and at a thinner loess section, and as such it is not known to what degree this variability may have affected their results. Furthermore, given that only six aliquots per sample were analysed in Clarke et al. (2007), it is hard to examine the nature or cause of De variability between aliquots in that study. Here some inter-aliquot aliquot De variability is seen (Appendix A), particularly in the upper loess unit, which may cause enhanced scatter in ages, especially with lower numbers of aliquots. Finally, while phases of dust accumulation ought to at least be locally consistent, the different location and thickness of the sites may have also played a role in age differences in the studies.

Thus, while the causes of the age offsets between the results here and in Clarke et al. (2007) are unclear at present, water content estimation and inter-aliquot variability are likely to be contributing factors. A high sampling resolution approach to age dating, coupled with Bayesian modelling, as employed here is required to assess the true age of the loess units (as outliers are more easily identified). Our new ages are more in line with recent age estimates from western continental European loess deposits, and would therefore fit better with proposed linked models of transport and deposition of loess in both areas (Antoine et al., 2009, 2016; Schaffernicht et al., 2020), as well as with suggestions that the Kent loess deposits mark the westerly end of the European loess (Perrin et al., 1974; Lill and Smalley, 1978; Antoine et al., 2003).

5.2. Sediment properties

Grain-size analysis shows that the distributions typically fall into the 'loess sediments in the medium to coarse-grained silt fraction' defined by Vandenberghe (2013). The Pegwell Bay loess is similar but slightly coarser than loess in NW and central Europe (Vandenberghe, 2013), implying a comparatively close by source. Fig. 4 and S7 show that Pegwell Bay loess has relatively high U-ratio values and high sand contents (10–30%), again supporting this assertion. The geochemistry (Fig. 4 and S8) shows generally typical loess characteristics, although it is greatly affected by the transition between calcareous to non-calcareous loess at c. 1.8 m. Weathering indices (Fig. 4 and S9) are hard to compare to published data due to differences in machine accuracy, calibration and protocol applied, yet are relatively low compared to loess in central and eastern Europe (Buggle et al., 2011), although they increase substantially in the non-calcareous loess unit. As carbonate buffers against silicate weathering (Gocke et al., 2014), this abrupt increase is likely due to the lack of carbonate in the upper unit.

Magnetic mineralogy appears complex at the site. The Day plot (Fig. 5C) shows a mixture of single domain and multi domain (or

PSD) magnetic grains in the loess, similar to the results reported from various loess profiles globally (Liu et al., 1992; Fukuma and Torii, 1998; Lagroix and Banerjee, 2002; Pan et al., 2002; Li et al., 2018; Taylor et al., 2014; Necula et al., 2015). Fukuma and Torii (1998) and Necula and Panaiotu (2012) observed decreasing Hcr/Hc ratio in palaeosol horizons as compared to sediment units, similar to the differences observed between Group 1 and 2 here (Fig. 5C; loess (Group 1) and upper soil (Group 2)). This was considered to be a result of pedogenic processes, such as mineral neoformation and weathering. Interestingly, the calcareous loess tends to lie closest to multi-domain (MD) dominance on the SD (single-domain)-MD mixing line, suggesting very limited post depositional weathering, in agreement with weathering proxies (Fig. 4). As with many loess deposits (Maher, 2011, 2016), the dominant magnetic mineral carrier appears to be magnetite, as shown in the clear drop in magnetization during heating to the Curie temperature (Tc) of magnetite (585 °C) (Fig. 5D). Generally, the magnetic proxies tend to show increasing finer grain magnetic mineral content with decreased depth (Fig. 4). Xlf and χfd show increases broadly from the base of the non-calcareous loess unit, accelerating to the upper soil, implying increasing MD, SD and superparamagnetic (SP) particle abundance up section. However, χlf peaks below the soil, while χfd peaks within the soil, suggesting that SP particles have a relatively small influence on the χlf signal.

Some further insight into the cause of formation of susceptibility signals in loess can be obtained through plotting χlf versus frequency dependence (Zeeden et al., 2016, 2018). Fig. 5A shows that the PB samples generally plot to the left of the so called 'true loess line'. This line denotes the pathway of magnetic enhancement under the classic pedogenetic enhancement model applicable to loess in areas such as central Europe and the Chinese Loess Plateau. Samples plotting to the left of the line may indicate that the 'wind vigour' model (Begét and Hawkins, 1989; Maher, 2011) may apply, whereby magnetic susceptibility enhancement may be driven more by greater wind speeds blowing in increased amounts of coarser, MD ferromagnetic grains that enhance χlf rather than frequency dependence. This certainly seems to apply to the samples from the lower calcareous loess unit (yellow in Fig. 5A), which show low values of both parameters and a steep line of χlf increase. By contrast, the upper non-calcareous unit samples (orange-red in Fig. 5A) show a shallower line of increased parameter values, which may suggest some pedogenic enhancement but may also indicate hydromorphic alteration of magnetic minerals under redox conditions, leading to dissolution of magnetic particles (Bábek et al., 2011; Baumgart et al., 2013; Fischer et al., 2017). Samples from the upper soil (brown in Fig. 5A) show closer alignment to the true loess line suggesting that this unit alone may be explained by the pedogenic enhancement model. Support for this comes from the analysis of magnetic susceptibility under multiple frequencies (Fig. 5B). While the soil sample (PB60) shows a similar trend to the Chinese Loess Plateau sample (albeit with considerably lower absolute susceptibility), the two samples from the calcareous and non-calcareous units (PB260 and PB140 respectively) show a distinctly shallower slope of susceptibility loss with frequency increase. This implies greater control of MD particles on the susceptibilities of these loess samples.

The upper soil deserves some further comment. Weir et al. (1971) and Wintle and Catt (1985) report a buried (by colluvium) mid-Holocene soil further north of the sample section, which may be equivalent to parts of the upper soil here. The luminescence ages here are clearly affected by recent processes in the upper 50 cm of the profile, yielding ages c. 1.6 ka and younger (Fig. 2). This is quite consistent with results from a wide range of loess soils where burrowing, bioturbation, and other soil forming processes may have mixed sediments from the surface to lower levels and caused depositional age underestimates (Bateman et al., 2007; Stevens et al., 2007). However, the age of 11.9 ± 0.8 ka from the base of the soil leaves the possibility open for ongoing slower deposition of loess after the main phases of loess accumulation prior to 18 ka (Fig. 2). While it is plausible that this c. 12 ka age may be an underestimate of the depositional age due to the influences mentioned above, it could also point to loess accumulation carrying on into the late phases of the last glacial, and even the Younger Dryas (Dimlington stadial; 12.9 to 11.7 ka). It is noteworthy that this age point lies above the first χlf peak that may indicate a Dansgaard–Oeschger event 1 (DO-1; sometimes referred to as 'Bølling' in previous work) palaeosol at the section (see online Appendix), tentatively supporting an argument for Younger Dryas loess and DO-1 soil formation at the site. As such, there may have been three recorded stages of soil formation affecting the upper part of the studied profile: an early phase during the DO-1 interstadial when loess was still accumulating, a main Holocene phase of soil formation including clay eluviation, and a more recent phase of reworking of the upper part of the soil. This requires further study but the effect of soil formation on the upper non-calcareous loess unit is discussed below (5.3).

5.3. What caused the abrupt boundary between the upper and lower loess units?

The cause of the sharp boundary between the two loess units at Pegwell Bay (and Ospringe) has been a source of much controversy. Traditionally, the upper non-calcareous loess unit has been interpreted to be a decalcified horizon of the argillic brown earth Holocene soil (Pitcher et al., 1954; Weir et al., 1971), in line with observations from other Holocene soils developed on loess and Quaternary sediments in southern Britain (Rose et al., 2000; Catt, 2008). However, Clarke et al. (2007) reinterpreted the upper loess unit as representing a separate phase of dust accumulation with a different (non-calcareous) dust source, separated by a hiatus. This reinterpretation rested on the basis of their luminescence dates, morphological evidence of rhizolith cut off at the boundary, and differing stable isotope composition of rhizoliths from the two loess units at Ospringe. Clarke et al. (2008) argued that there is also a change in mineralogy and clay mineralogy across the boundary, with the lower calcareous unit showing lower quartz contents but greater smectite abundance. They also suggest that the lower unit has a higher proportion of corroded feldspars and angular quartz grains than the upper unit. On the basis of detailed mineralogical and petrological investigation of the two units at Pegwell Bay and Ospringe, Milodowski et al. (2015) modified this idea by arguing that the upper unit was in fact a solifluction deposit. In particular, the upper non-calcareous loess differs from the lower calcareous loess in that the latter shows an open-packed arrangement of clay coated grains where illuviated clay builds bonds between the grains. The upper unit by contrast shows a close-packed interlocking grain arrangement indicative of mass movement destroying any pre-existing delicate grain-bridging microfabrics. However, Catt (2008) questioned the luminescence dating evidence and argued both rhizolith truncation and isotopic evidence are still consistent with soil formation and a decalcification front under Holocene pedogenesis.

Assigning a regional unconformity based on only two luminescence ages per section is speculative, especially when the ages for the boundary do not overlap at two different sites. The high sampling resolution luminescence dating results here show no obvious jump or transition that would indicate an unconformity between the two loess units (Fig. 2). However, given the uncertainty in the individual ages and the scatter in ages between 2.3 and

1.5 m depth, a short (of the order of 1–2 ka) episode of non-deposition could be possible, but remains entirely speculative. Furthermore, there is no obvious abrupt shift in mineral magnetic parameters at this level (Fig. 4), which tend to show only gradual changes (if any), particularly a gradual increase in MD grain abundance up section. While there is a temporary grain-size spike at or just below the boundary (Fig. 4), there is only a minor consistent increase in grain-size (driven by greater sand content) above the boundary. In contrast, there are significant differences in dose rate (Fig. 2) and geochemistry (Fig. 4, S8 and S9) between the two units. Apart from the clear drop to near zero CaO contents, mobile oxides and elements decrease substantially upwards across the boundary, while weathering indices and less mobile or immobile elements increase or show no consistent pattern. Leaving aside the initial cause of the CaO difference, these other patterns can be explained simply by enhanced silicate weathering in the upper unit (Buggle et al., 2011). At first glance, this would seem inconsistent with a decalcification front in a single soil (given the 19–24 ka proposed age for the loess) but because carbonate buffers against silicate weathering this increased apparent weathering may purely be a function of the lack of carbonate in the upper unit (whatever the cause of that). Certainly, the mineral magnetic parameters do not show any evidence of abrupt changes in weathering at the boundary, and are more indicative of competing effects of wind-vigour and redox conditions on mineral magnetic signals in the upper unit (Fig. 5). No clear change in element ratios associated with source changes can be seen at the boundary (Ti/A and Ti/Zr) and in contrast to Clarke et al. (2007; 2008), no substantial shift in SiO_2 content is observed across the boundary (although fluctuations in these values in the lower unit seem related to changes in sand content; Figures S8 and S9).

Much of the evidence above lends little direct support for the proposals of differently sourced dust deposition phases separated by erosion (Clarke et al., 2007), or solifluction of the upper loess unit (Milodowski et al., 2015). Particularly, the luminescence ages are not consistent with a long erosional break or reworking due to solifluction. While age modelling suggests two phases of enhanced dust accumulation (see section 5.5), these phases are not strictly stratigraphically associated with the unit boundary. Furthermore, the gradual or lack of changes in most sediment properties across the boundary suggest neither reworking nor a change in source. The increased silicate weathering in the upper loess unit is best explained simply by the lack of carbonate in that unit, whatever the cause. However, the previously published finding of different particle packing properties is compelling evidence for some fundamental difference in process affecting the two units (Milodowski et al., 2015), and is not easily explained by brown earth soil formation. Furthermore, while there is a gradual increase in magnetic susceptibility up profile in the upper non-calcareous loess unit, this is better explained under a wind vigour model rather than pedogenesis (although it could also suggest a change in dust source). In addition, the slight increase in grain-size in the upper unit, and grain-size spike at the boundary between the two units implies a slight shift in environment between the two units.

To reconcile these seemingly competing observations we propose that another process may have caused the boundary at the site. From c. 27 to 21 ka continuous permafrost was a feature of southeast England (Murton and Ballantyne, 2017), coincident with the main phases of loess deposition reported here. Following approximately 21 ka there was a shift to discontinuous permafrost, while analysis of periglacial features in deposits in Thanet, Kent, point to active layer thickening to c. 2 m from c. 21 ka (Murton et al., 2003). Prior to this, the active layer was likely very thin, due to the very cold arid climate at the time. Indeed, although other parts of the BIIS had already retreated from their maximum extent, the North Sea Lobe part of the BIIS began a major retreat phase after c. 21–20 ka (Roberts et al., 2018), which may have allowed more warm, moist air masses into southeast Britain. We suggest therefore that an explanation for the differences between the two loess units could be related to this phase of active layer deepening. The depth of the boundary (c. 1.8 m) between the two loess units is consistent with a maximum 2 m thick active layer depth at this point, while the closely packed particles in the upper loess unit (Milodowski et al., 2015) could be explained by hydroconsolidation during water logging in an active layer. When saturated or wet, loess deposits are susceptible to hydroconsolidation, a structural change from an open particle packing to a closer particle packing (Dijkstra et al., 1995; Smalley and Markovic, 2014). During this collapse, pre-existing delicate bonds between grains are broken down and void space is reduced in the non-calcareous unit (Milodowski et al., 2015), which might also explain the field observation that the loess from this unit tends to break in columnar blocks. The seasonally thawed but saturated active layer would also explain the lack of evidence for pedogenic mineral magnetic enhancement of the upper loess unit, and fit with hydromorphic dissolution of ferromagnetics during water logged conditions (Fig. 5). Moreover, the perennially frozen permafrost would be impenetrable for plant roots and explain “rhizolith cut off” at the boundary and differing isotopic composition of rhizoliths from the two loess units (Clarke et al., 2007). Finally, the lack of carbonate in the upper loess unit can be explained by decalcification in the active layer. Leaching of Na, Mg and Ca cations has been shown to occur in active layers of silty soils, leading to abrupt increases in Na and Ca concentrations in the perennially frozen ground below (Kokelj et al., 2002). Once decalcified, sediments are extremely susceptible to silicate weathering, even under cool conditions (Gocke et al., 2014), accounting for the geochemical and weathering indicator changes down the Pegwell Bay profile. While most of the loess at Pegwell Bay may have been deposited rapidly under cool climate conditions, it is also possible that the later period of loess deposition (see 5.5) occurred broadly coevally with this active layer deepening, and weathering. This explanation would also account for the regional nature of the boundary, a feature hard to explain by localised solifluction processes. Furthermore, some of the variability in grain-size and luminescence age within the upper loess unit may be explained by mixing in the active layer. Indeed, analysis of sample aliquot De distribution shows the upper loess unit generally exhibits more scatter in aliquot De than the lower calcareous unit (Appendix A; Table S1; Fig. S4), which may be related to post depositional mixing under active layer conditions. Subsequent DO-1/Holocene soil formation would have then overprinted the upper part of the decalcified loess unit, accounting for the mineral magnetic properties in the upper soil. Under this model full retreat of permafrost conditions at the site during the DO-1 event would have rapidly lowered the active layer boundary down into the underlying sandy Thanet Formation, leading to well drained conditions at the site that prevented further hydroconsolidation of the lower loess. It is unclear whether Pegwell Bay would have experienced further permafrost conditions during the Younger Dryas, as only discontinuous permafrost occurred at that time (Murton and Ballantyne, 2017). In any case, it is likely that any subsequent deepening and disappearance of the active layer would also have been rapid at the Holocene onset. We therefore argue that this hypothesis is currently the most parsimonious explanation of the diverse range of evidence from above and below the boundary presented here and in previous work, but underscore that the idea requires further testing.

5.4. Palaeoclimate reconstruction

Given the relatively short time frame covered by the loess accumulation at Pegwell Bay, the dry climate during the initial depositional phase, and the potential for overprinting of any dust depositional contemporaneous environmental information recorded at the site under active layer deepening, it seems hard to obtain records of past climate change from proxies in the sequence. Fig. 3 shows variation in selected proxies over the main depositional interval at the site. In addition to dust MAR and particle size data, key mineral magnetic parameters are included, notably the maghemite proxy based on thermomagnetic experiments. We suggest that this proxy may indicate the neoformation of maghemite, likely as coatings on larger MD magnetite grains, and therefore occurring in smaller magnetic grain size (SD and PSD). Peaks in the proxy then may indicate short periods characterized by slightly humid and a more moderate climate, favouring weathering and forming of such fine grain maghemite.

Dust MAR and grain-size data may be heavily affected by regional synoptic patterns and sediment supply/availability, as discussed below (5.5). As such, they are hard to use as palaeoclimate proxies here. Xlf data likely reflects changes in wind vigour (see section 5.2), but is probably also a function of dust availability, source characteristics and proximity in relation to wind directions. Xfd shows little variation beyond a gradual increase towards the Holocene soil (Fig. 4). Clearly, any pre DO-1/Holocene amelioration in climate during the depositional phase was not sufficient to drive a response in weathering-driven SP grain formation, or active layer processes inhibited any such response. The CPA index is heavily affected by active layer deepening and below this the only changes in the record appear related to changes in grain size (Fig. 4). The maghemite proxy however shows three peaks over the depositional interval (grey areas in Fig. 3). These may indicate slightly enhanced weathering phases and indeed these peaks are also shown in Fe_2O_3 oxide ratios to a greater or lesser degree. Hcr/Hc and ARM proxies show a more complex relationship but the middle and younger peaks broadly match the maghemite % peaks. Ti/Zr ratio partly shows variation in tandem with grain-size, and the oldest of the three maghemite peaks matches an increase in sand content. It is unclear if there is a causal relationship between this grain-size peak and weathering. The youngest maghemite peak is also coincident with a change in Ti/Zr, but this time, of the opposite sign (Fig. 3). This is also coincident with the large increase in dust MAR after 20 ka.

Clearly interpreting these changes is complex, but we here postulate that the maghemite proxy and Fe_2O_3 oxide ratios at least, are indicative of slightly enhanced weathering at c. 23 ka, c. 21 ka, and 20–19.5 ka, unrelated to changes in dust deposition and associated chemical and grain-size shifts. The change at c. 23 ka is broadly coincident with GI-2 in the Greenland ice cores, a short period of warming and lower dust accumulation (Rasmussen et al., 2014). The following GS-2 stadial lasted until c. 14.5 ka but a slightly warmer phase (GS2.1) occurred from 21 to 17.5 ka, and may be linked with the younger two weathering peaks. However, it is likely that regional shifts in tracking of precipitation bearing storms (see section 5.5) may have been more important in driving weathering at the site, and uncertainty on the Pegwell Bay age model of c. ±1 ka prevents any easy association of these peaks with specific short-term climate events. We suggest that the maghemite proxy shows promise in examining high frequency yet low amplitude shifts in weathering during generally arid phases, but requires testing on even better age constrained sequences, for example on extremely detailed ^{14}C dated loess records like at the Dunaszekcső loess sequence in southern Hungary (Újvári et al., 2017).

5.5. The timing of dust deposition and link to ice sheet dynamics

Clearly, the luminescence ages presented here show very quick deposition of a 3–4 m thick loess deposit over a relatively short time frame (Fig. 2). Scatter in the ages between 230 and 150 cm is discussed in Appendix A, but Bayesian modelling allows construction of a continuous age depth model based purely on these luminescence ages and prior stratigraphic information (Blaauw and Christen, 2011). The resultant dust MAR values are plotted by age model age in Fig. 3, and show two abrupt increases in the rate of dust accumulation centred on c. 25–23.5 ka and c. 20–19 ka, with lower rates of accumulation between these two peaks, and potentially following 19 ka. Notably, there is no evidence of loess accumulation at the site prior to 25 ka. The peak dust mass accumulation rates here (Fig. 3) are large compared to previously published estimates of peak last glacial dust MAR from luminescence dated loess sequences in China and Europe (Kang et al., 2015; Stevens et al., 2016; Peric et al., 2019), although slightly lower than peak values reconstructed from Hungarian loess using a radiocarbon chronology (Újvári et al., 2017). While differences in the absolute values of MAR are highly dependent on age model resolution and choice of age modelling procedure, and have substantial uncertainties on the absolute sizes of MAR peaks, this in any case suggests two very active phases of dust accumulation at Pegwell Bay during the peak last glacial. The timing of the first peak coincides with Heinrich event 2 (Hemming, 2004), a period of greatly enhanced dust activity (GS-3) recorded in the Greenland ice cores (Rasmussen et al., 2014), peak loess deposition across the Chinese Loess Plateau (Kang et al., 2015; Stevens et al., 2016), enhanced dust accumulation in the Pacific (Hovan et al., 1989), and greater loess accumulation in central Europe (Stevens et al., 2011). The first accumulation pulse at Pegwell Bay is therefore part of globally enhanced atmospheric dustiness over the Heinrich event 2 and GS-3 interval. In addition, ice rafted debris records show that most ice streams of the BIIS all show common maxima just before Heinrich event 2, with pull back from these mostly marine terminating maxima, resulting in increased ice berg flux (Scourse et al., 2019; Ó Cofaigh et al., 2019; Chiverrell et al., 2020).

Differing atmospheric regimes have been proposed to prevail over Europe during the last glacial when ice sheets approached their maximum extents, including easterly winds caused by the high pressure over the Eurasian ice sheet (COHMAP Members, 1988; Ludwig et al., 2016) and extreme cyclones tracking over central Europe deflected southwards by the aforementioned high pressure system (Antoine et al., 2009; Pinto and Ludwig, 2020). Recently, Schaffernicht et al. (2020) evaluated the contribution of these different atmospheric regimes to the last glacial dust cycle and concluded that east sector winds prevailed over central Europe 36% of the time, and cyclonic weather type regimes 22%. However, it is likely that the predominance of east sector winds was even more drastic for regions proximal to the ice sheet such as southern Britain. Furthermore, Lefort et al. (2019) propose katabatic winds as explaining loess distribution along the English Channel.

Below and in Fig. 7 we outline a model explaining the observed timing of loess accumulation at Pegwell Bay. During the time of loess deposition (c. 25–19 ka; Fig. 7B and C), the BIIS was connected to the FIS (Hughes et al., 2016; Roberts et al., 2018) leading to greatly enhanced katabatic winds (Krinner et al., 2004; Lefort et al., 2019) and a westward expansion of the Eurasian ice sheet high pressure system (Lill and Smalley, 1978; Schaffernicht et al., 2020). The resultant strong northeasterly/easterly winds over Southern Britain and the North Sea area would have provided ideal conditions to entrain sediment from the exposed North Sea shelf and braided river systems, and subsequently transport the material

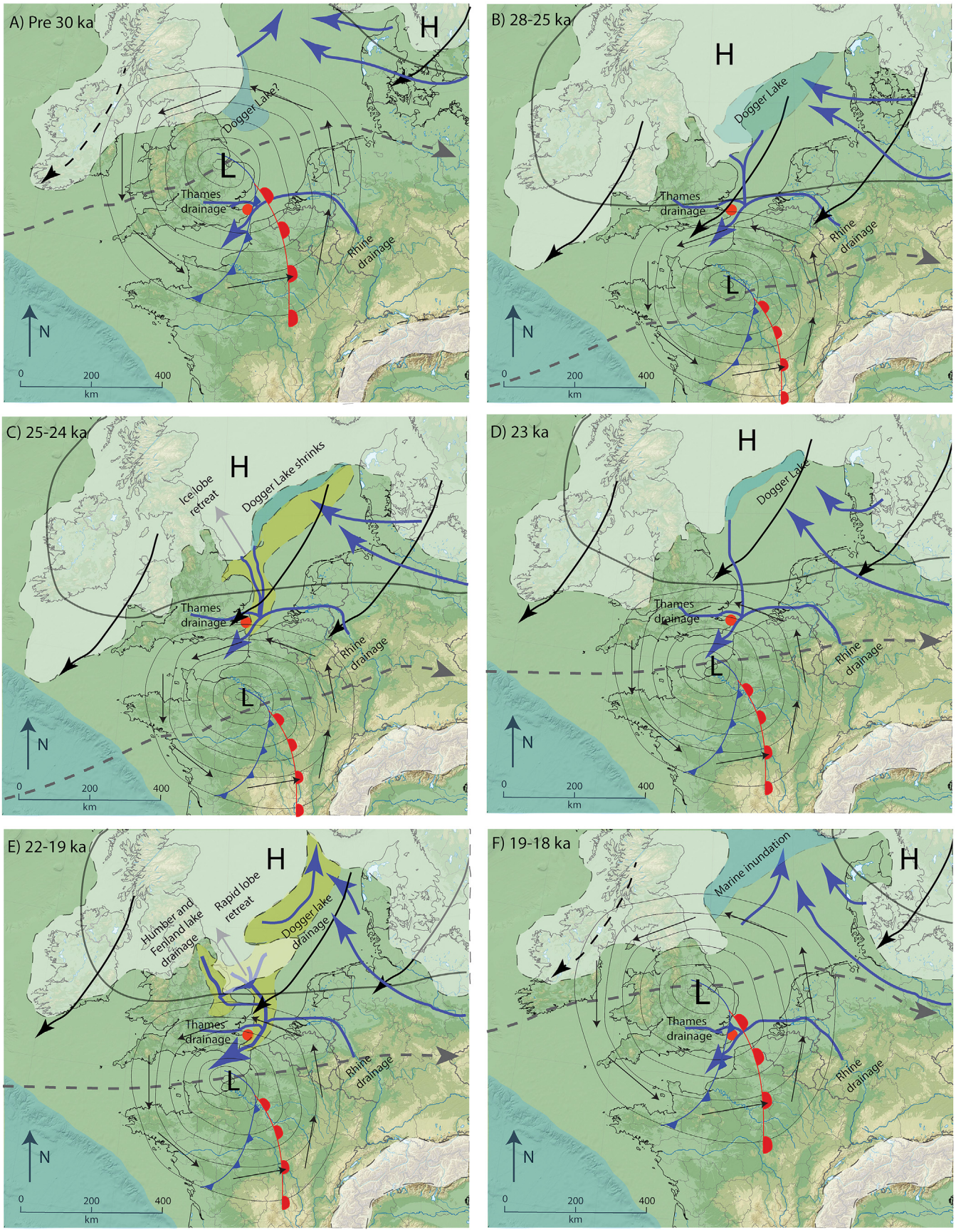

Fig. 7. Schematic model of NW Europe ice sheet extent, dominant dust transporting atmospheric conditions and likely North Sea basin drainage over six intervals of the last glacial (based on Antoine et al., 2009; Hughes et al., 2016; Stroeven et al., 2016; Smedley et al., 2017; Chiverrell et al., 2018; Roberts et al., 2018; Seguinot et al., 2018; Scourse et al., 2019;

westwards to SE England. Moreover, the shielding effect of the high pressure over the Eurasian ice sheet would have diverted Atlantic depressions (Schaffernicht et al., 2020) and prevented transport of moist air into regions close to the BIIS. The resulting environment would have been extremely cold, dry and windy, as reflected by the Pegwell Bay proxy record, indicating pure loess deposition without post depositional alteration (Fig. 3). The Atlantic depressions tracking to the south of Pegwell Bay (Fig. 7B and C) would have also caused strong, gusty easterly winds tracking from North Sea basin dust source areas westwards over Southern Britain (Antoine et al., 2009; Pinto and Ludwig, 2020). Antoine et al. (2009) explain the extremely high last glacial dust accumulation between 30 and 20 ka at the Nussloch site in western Germany, as well as the association of loess and aeolian sands in Western Europe generally, by this tracking of dust storms through the English Channel and over NW Europe (Fig. 7). Recent climate modelling also points to enhanced cyclonic activity over Western Europe during the last glacial maximum at peak European Ice Sheet extent, with extreme cyclones characterized by greater wind speeds and lower precipitation in comparison to pre-industrial cyclones (Pinto and Ludwig, 2020). Combined with extensive loose silt-size sediment availability, this would have driven extensive dust storm activity.

However, given that there were also earlier, substantial dust accumulation peaks in Greenland and central European dust records (Rasmussen et al., 2014; Újvári et al., 2017; Peric et al., 2019), this raises the question as to why there was no loess accumulation at Pegwell Bay prior to 25 ka. It is possible an erosional event removed pre-existing late Quaternary loess, but this would seem inconsistent with the rapid, continuous accumulation from c. 25 ka (Fig. 2). An alternative explanation may lie in the relationship between the dynamics of the BIIS, atmospheric circulation, sediment supply and availability, North Sea drainage and the coupling of the BIIS and FIS (Fig. 7A). Prior to 28–25 ka, the BIIS did not reach as far south as its fullest extent and more importantly it was an isolated ice sheet covering only the north of Britain and Ireland, disconnected from the FIS (Hughes et al., 2016; Roberts et al., 2018) (Fig. 7A). Under this situation we propose that the Eurasian ice sheet related high pressure system would have remained east over Scandinavia, rather than extending over the British Isles. This would have led to far less influence from polar easterlies at Pegwell Bay than later during BIIS coalescence (compare Fig. 7A with 7B). Furthermore, the southern North Sea would have been mostly ice free, inhibiting the generation of katabatic winds. Combined, the strong easterly winds required for dust entrainment from the exposed shelf and loess deposition over southern Britain were greatly reduced. In addition, given the north-eastward position of the high pressure system over the Eurasian ice sheet towards Scandinavia, cyclonic regimes dominated dust emission and deposition over Europe more generally (Pinto and Ludwig, 2020). However, the resulting westward dust transport over central and eastern Europe (Schaffernicht et al., 2020; Antoine et al., 2009) still favoured dust deposition in these regions (Újvári et al., 2017), and polar easterlies would still have been important for dust transport in areas to the south of the FIS. By contrast, the predominating winds and wetter climate associated with these eastward tracking depressions over Western Europe inhibited dust fall over southern Britain. Southerly flow on the back of these depressions could still have deflated and transported dust from the exposed North Sea and Channel to Belgium, France and Germany (Antoine et al., 2009; Schaffernicht et al., 2020), but less easily to Britain.

If this model is true then dust deposition over southern Britain is tied to winds associated with a semi-permanent high pressure system and katabatic winds forming over the converging BIIS and FIS, and the subsequent impact on Atlantic depression storm tracks. However, a question this explanation raises is why there was particularly enhanced dust accumulation at Pegwell Bay during two specific short phases (25–23.5 ka and c. 20–19 ka) of the last glacial, after the BIIS and FIS has coalesced. We propose that the dynamics and drainage of the North Sea Lobe (NSL) and associated glacial lake Dogger (Roberts et al., 2018) may have controlled sediment supply and availability in the southern North Sea, and therefore these phases of loess deposition. The NSL attained its first maximum around 28–25 ka, and acted to dam up much of the central southern North Sea, forming glacial lake Dogger (Roberts et al., 2018) (Fig. 7B). Retreat of the NSL and initial part drainage of Dogger Lake immediately after this maximum, would have released massive amounts of sediment and meltwater southwards immediately northeast and east of Pegwell Bay, and into the Channel River, as well as exposed a large sediment rich former lake bottom (Fig. 7C), acting as a new sediment source of loess formation (yellow area Fig. 7C). This also coincides with a European Ice Sheet meltwater pulse along the Channel River at the same time as Heinrich event 2 (Toucanne et al., 2015), as well as retreat of marine margins of the BIIS (Scourse et al., 2019: Ó Cofaigh et al., 2019; Chiverrel et al., 2020). The first enhanced phase of accumulation may also be explained by the position of the storm tracks being controlled by sea ice and ice sheet extent (Pinto and Ludwig, 2020). Although the exact timing of the maximum advance of the different parts of the BIIS is uncertain, the maximum advance of the Irish Sea Ice Stream in the southwest of the BIIS coincided with Heinrich event 2 (Smedley et al., 2017; Scourse et al., 2019) (Fig. 7B and C). Retreat of this feature was rapid (Scourse et al., 2019) (Fig. 7D), and by the time of the second peak of dust accumulation at Pegwell Bay the ice stream lay as far north as Anglesey-southern Isle of Man, (Chiverrell et al., 2018). The time of the ice stream advance coincides with the first phase of loess deposition at Pegwell Bay. We propose that without this ice stream advance it is likely that depressions tracked further north, especially when the Eurasian ice sheet high pressure system was restricted further east (Fig. 7A and F), meaning that more westerly dominated boundary layer flow would have occurred, reducing direct transport of sediment from the main North Sea basin dust source areas to south-eastern Britain, and increasing moisture transport to the region. Thus, the presence of the ice stream in the west of the BIIS during Heinrich event 2 (Fig. 7C) may have enhanced the first phase of accelerated loess build up at Pegwell Bay.

This explanation raises the question as to why the second peak in dust accumulation occurred at c. 20–19 ka, during retreat of the western BIIS and decoupling of the eastern BIIS from the FIS. While the early part of this second enhanced accumulation phase may have coincided with a coupled FIS and BIIS situation outlined above (Fig. 7E), the return to decoupled ice sheets would have led to

Pinto and Ludwig, 2020; Schaffernicht et al., 2020). Very approximate sea level and former Dogger Lake area is shown in blue and ice sheet size and extent is approximate given chronological uncertainties. Ice sheets are shown in white, while North Sea basin drainage directions are shown with blue arrows with key aspects marked. Pegwell Bay is shown by a red dot. Storm tracks are shown by grey dashed arrows while approximate representations of low (L) and high (H) pressure systems are shown with lines, and with black arrows denoting wind directions. A) Pre 30 ka and B) 28–25 ka shows situation just prior to loess accumulation at Pegwell Bay, while C) 25–24 ka and E) 22–19 ka show the situations at the two enhanced loess accumulation peaks at Pegwell Bay (section 5.5). D) 23 ka shows the situation between the two peaks and F) 19–18 ka shows the situation after enhanced loess accumulation has ceased at Pegwell Bay. Areas where extensive exposed former lake sediments or strong glaciofluvial outwash sediments are suddenly available are shown in light yellow shading for C) and E). These are possible loess source areas during the enhanced depositional phases at Pegwell Bay at those times. (For interpretation of the references to colour in this figure legend, the reader is referred to the Web version of this article.)

decreased influence of polar easterlies and katabatic winds, as well as caused storms to track further north (Fig. 7F). This would have reduced the dust transporting easterly winds required for loess accumulation over southern Britain and enhanced moisture penetration over the region, inhibiting loess deposition at Pegwell Bay. However, just prior to the second peak in loess accumulation, the NSL surged and reached its full extent, impinging on the north Norfolk coast (Figs. 1 and 7E; Roberts et al., 2018). This occurred rapidly around 22–21 ka, resulting in substantial build-up of ice dammed lakes over eastern southern Britain (Evans et al., 2019) as well as damming of extensive amounts of FIS and BIIS meltwater (Patton et al., 2017). Decay of this lobe was also abrupt, occurring between 21 and 19 ka (Roberts et al., 2018), and was linked to drainage of glacial lakes Humber and Fenland, as well as with final demise of Dogger Lake, as the FIS and BIIS decoupled. The retreat coincides with the proposed second dust accumulation peak at Pegwell Bay (Fig. 3). We propose here that, as with the first phase of loess accumulation, a sudden new input of NSL/BIIS meltwater would therefore have occurred in the southern North Sea at c. 21–19 ka, passing directly north and east of Pegwell Bay. This would have been augmented by substantial volumes of released ice dammed lake water from glacial lakes Humber and Fenland, radically changing the hydrological conditions in the basin adjacent to Pegwell Bay and southern Britain (Figs. 1 and 7E). We further propose that this event would have been accompanied by a large injection of sediment from the BIIS and ice dammed lakes into the southern North Sea. Such a catastrophic pulse of material input would have drastically altered the landscape of the southern North Sea, and resulted in the sudden availability of substantial volumes of unconsolidated sediment, especially as meltwater levels dropped and exposed sediment rich and vegetation poor braided channels immediately east of southern Britain. Pegwell Bay lies very close to these sediments (Figs. 1 and 7) and thus even infrequent easterly, northeasterly and southeasterly winds would have delivered greatly increased volumes of windblown silt to the site, consistent also with increases in grain-size up section (Fig. 4). However, an advanced NSL position may also have enhanced northeasterly katabatic flow over Pegwell Bay, providing a means to transport sediment from the North Sea basin early on in the NSL decay, and a large area of sediment rich glacial lake sediment would have been exposed upon drainage of north east English and Dogger glacial lakes (Fig. 7E). This second pulse of sediment would have occurred when the BIIS was reduced in extent compared to the first pulse (Fig. 7), and coincides with a change to discontinuous permafrost at the site (Murton and Ballantyne, 2017). Reduced ice volume would likely allow wetter, potentially warmer, conditions during and immediately following accumulation of second phase of enhanced dust accumulation, due to greater penetration of North Atlantic depressions over southern Britain (Fig. 7F).

Clearly this needs further testing, but we note that our hypothesis is consistent with active layer deepening coincident with, or just following, the second enhanced dust accumulation phase, as proposed above. A large part of the second phase of dust accumulation coincides stratigraphically with the non-calcareous loess (Fig. 2 and S1) and while the calcareous loess to non-calcareous loess transition is not in itself a function of changing source under this scenario (which as pointed out by Catt (2008) would be very unlikely in a region rich in carbonates generally), it broadly coincides with the different dust accumulation phases (Fig. 2) and records a deepening of the active layer that is linked to the climate changes driven by BIIS dynamics. The tracking of depressions further north over southern Britain (Fig. 7D) would (Evans, 2001) have brought warmer and more humid air to the area, as southern Britain became influenced by high precipitation frontal areas in the centre and south of depressions. Existing heavy mineral assemblage and particle size data from loess in Britain also suggest a genetic link with ice sheet sediment sources in the North Sea for the east of England and easterly wind sediment transport (Catt and Staines, 1982; Bateman and Catt, 2007), although detailed provenance analyses are needed to test this model further, particularly in terms of changing sources through time. Furthermore, analysis of submarine geomorphology, stratigraphy and sediment age in the southern North Sea reinforces evidence for potentially multiple megafloods during the last glacial, driven by glacial lake outbursts in the North Sea, or rapid ice sheet melting in the catchment (García-Moreno, 2017; De Clercq, 2018; García-Moreno et al., 2019). These floods may have been driven by drainage of Dogger Lake, with meltwater channelled southwards to the Channel River via the Axial Channel of the Southern North Sea, immediately east and northeast of Pegwell Bay. Provenance, shape and size analysis of large clasts on the Belgian continental shelf associated with flooding events suggest a link with the BIIS, and require extremely high fluvio-hydraulic transport energy (De Clercq, 2018). Indeed, the proposed lake at the southern margin of the FIS and BIIS in the North Sea would have dammed up considerable volumes of meltwater from a drainage area extending to Northern Scandinavia and Poland (Patton et al., 2017). Drainage of this lake would also have transported considerable volumes of finer material, acting to enhance sediment supply, and after flood level decreased this material would become available for aeolian deflation to loess.

We therefore propose that the western and eastern BIIS ice stream and lobe advance and retreat patterns, as well as the coalescence of the FIS and BIIS during the late last glacial, explain the observed dust accumulation pattern at Pegwell Bay. The impact of the ice sheets on sediment supply and atmospheric circulation, as well as the topography of the exposed North Sea, and the position of southern Britain to the west and north of the main dust sources (Fig. 7), led to a highly constrained period of loess accumulation at the site, coincident with the peak European ice volume and early deglaciation. It is particularly striking how the dynamics of the NSL during coupling and decoupling of the BIIS and FIS match changes in loess accumulation, via its control on North Sea drainage, sediment supply and availability. This proposal may also serve as a model explaining the occurrence of loess in southeast Britain generally, as well as its relatively thin nature and short duration of accumulation, in relation to deposits to the east and south over continental Europe. Given that the North Sea and Channel are likely sources for loess deposits over much of NW Europe (Sima et al., 2009), the pulses of sediment accumulation seen at Pegwell Bay ought also to be seen in other loess records in the wider area. This clearly requires testing on other loess sites using high-resolution independent age dating in both Britain and western continental Europe. However, few sites in NW Europe have been dated using high sampling resolution independent methods sufficient to analyse short term changes in accumulation rate (see Stevens et al., 2008 for discussion on this). Of the suitably dated records that do exist, it appears that greatly enhanced loess accumulation in NW France, Belgium and Germany also occurred during the upper last glacial (Antoine et al., 2016; Guérin et al., 2017; Zens et al., 2018). Although considerably further afield and likely to be sourced from Rhine material, the extremely well dated Nussloch site in central Germany also shows greatly enhanced accumulation rates between 30 and 20 ka (Moine et al., 2017). Furthermore, although recent absolute dating of coversands in the area has been limited, there appears to be a peak in sand accumulation roughly coincident with peak BIIS ice extent (Buylaert et al., 2009; Bateman et al., 2014). The deposition of dust via winds associated with storms is also consistent with the distribution of loess, not only in southern Britain, but also Belgium and Germany (Fig. 1) (Antoine et al., 2009),

although testing this model again requires considerably greater coverage of loess sites that have precise and accurate independent age models in NW European than exists at present. Furthermore, Lefort et al. (2019) argue for katabatic winds as explaining loess deposits in NW France. As such, while current well dated sites on NW Europe are consistent with the model presented above, detailed independent dating of multiple loess deposits across this area is required to fully test the influence of the BIIS on dust accumulation over NW Europe, and to test between Atlantic storm, katabatic, or ice sheet high pressure system winds in controlling loess deposition in the region. Our model also further emphasises the importance of understanding local conditions when reconstructing patterns and causes of shifts in atmospheric dustiness, and emphasises the need for detailed spatial coverage of independently dated dust records in order to simulate past atmospheric dust conditions (Albani et al., 2015). Peaks in dust accumulation at c. 25–19 ka are recorded in loess sediments across Eurasia (Stevens et al., 2011, 2016; Kang et al., 2015; Moine et al., 2017; Újvári et al., 2017; Peric et al., 2019), coincident with enhanced dustiness in Greenland ice cores (Rasmussen et al., 2014). However, the causes of this dustiness may be highly site specific, despite the overall more arid, windy climate of the last glacial.

6. Conclusions

Detailed quartz optically stimulated luminescence dating, mineral magnetic, grain-size and geochemical analyses of the loess deposits at Pegwell Bay, East Kent, UK, reveal a history of short-term dust deposition characterized by abrupt shifts in accumulation. We propose that this was driven by complex interplay of the British Irish Ice Sheet advance and retreat patterns and coupling to the Fennoscandian Ice sheet, the influence of this on sediment supply, Atlantic depressions and storm tracks, katabatic winds and ice sheet high pressure extent, and changes in active layer depth in a permafrost landscape. The loess at Pegwell Bay is likely deposited primarily under two main depositional phases centred on 25–23.5 ka and 20–19 ka. The first coincides with Heinrich event 2 and we propose enhanced dustiness is driven by enhanced sediment supply during initial decay of the North Sea Lobe and partial drainage of Lake Dogger. Furthermore, intense dust storms with easterly winds at the site would have been caused by enhanced polar easterlies, katabatic winds, and a southward shift of Atlantic depressions tracking over the English Channel during maximum western British Irish Ice sheet extent, the North Sea Lobe, and at coalescence of the British Irish Ice sheet and Fennoscandian Ice Sheet. The second enhanced dust deposition phase also occurred due to abrupt and dramatically enhanced sediment supply to the southern North Sea. This was driven by meltwater and released ice dammed lake water originating from the retreating North Sea Lobe of the British Irish Ice sheet that had previously advanced to the coast of North Norfolk. We predict that these events would have dramatically reshaped the southern North Sea drainage system and caused enhanced airborne sediment fall over wide areas of NW Europe. This later phase of enhanced dust accumulation broadly coincided with or slightly preceded a deepening of the permafrost active layer over southern Britain, causing the marked stratigraphic boundary between the upper non-calcareous and lower calcareous loess units at Pegwell Bay. This deepening may have been in part driven by greater penetration of warmer, wetter maritime air associated with northward movement of storm tracks after the retreat of the western BIIS after maximum extent at c. 24 ka. We propose that this model also explains the modest thickness of the southern British loess in comparison to continental deposits, as well as their generally westward (to East Devon) decrease in thickness and grain size. Only very specific conditions under maximum extent of the British Irish Ice Sheet, decay of the advanced North Sea Lobe, and coalescence with the Fennoscandian Ice Sheet would have been conducive for sediment supply coinciding with the strong, turbulent and dry easterly flow required to transport sufficient quantities of dust to southern Britain to drive loess accumulation. Our model requires testing at other sites across NW Europe, not only in terms of high sampling resolution independent age dating and modelling of dust mass accumulation rates, but also in terms of sediment source studies and atmospheric modelling. Our findings also shed light on the wider impact of changes in the size and shape of the British Irish Ice Sheet, and emphasise the importance of understanding local and regional conditions when considering modelling and reconstruction of past dustiness and associated climate impacts.

Author statement

TS conceived, designed and undertook the study. Fieldwork was undertaken by TS, RO and YB. DD, TS, GC, SA and VP all undertook and oversaw the luminescence dating, TS conducted age modelling, while TS, YB and DD undertook interpretation of the data with regard to ice sheet and permafrost dynamics. BB, TS and RO performed mineral magnetic analyses. Grain size and geochemical analyses were undertaken by RO and CT respectively. TS wrote the submission with help from DD, BB and YB, while all authors contributed to its revision and final version.

Declaration of competing interest

The authors declare that they have no known competing financial interests or personal relationships that could have appeared to influence the work reported in this paper.

Acknowledgements

We are grateful to the constructive comments of three anonymous reviewers, which have greatly improved the initial submission. We thank Professor Huayu Lu (Nanjing University) for the Lantian sample. This work was funded by the Swedish Research Council (VR grant 2017–03888) and the Quaternary Research Association (QRA) Quaternary Research Fund. BB acknowledges the financial support of project BU235P18 (Junta de Castilla y Leon, Spain) and the European Regional Development Fund (ERD). Financial support to SA, VP and DS is by LR7/2007 RAS Ricerca di Base (BANDO 2017) - Cambiamenti climatici e neotettonica – la Sardegna un continente semi-stabile (resp. VP). Partial funds to VP have also been provided by fondo di Ateneo per la ricerca “2019” and by the Russian Government Program of Competitive Growth of Kazan Federal University.

Appendix A. Supplementary data

Supplementary data to this article can be found online at https://doi.org/10.1016/j.quascirev.2020.106641.

References

Adebiye, A.A., Kok, J.F., 2020. Climate models miss most of the coarse dust in the atmosphere. Science Advances 6. https://doi.org/10.1126/sciadv.aaz9507 eaaz9507.

Albani, S., Mahowald, N.M., Winckler, G., Anderson, R.F., Bradtmiller, L.I., Delmonte, B., François, R., Gomanm, M., Heavens, N.G., Hesse, P.P., Hovan, S.A., Johfeld, K.E., Lu, H., Maggi, V., Mason, J.A., Mayewski, P.A., McGee, D., Miao, X., Otto-Bliesner, B.L., Perry, A.T., Pourmand, A., Roberts, H.M., Rosenbloom, N., Stevens, T., Sun, J., 2015. Twelve thousand years of dust: the Holocene global dust cycle constrained by natural archives. Clim. Past 11, 869–903. https://

doi.org/10.5194/cp-11-869-2015.
Antoine, P., Catt, J., Lautridou, J.-P., Sommé, J., 2003. The loess and coversands of northern France and southern England. J. Quat. Sci. 18, 309–318.
Antoine, P., Rousseau, D.-D., Moine, O., Kunesch, S., Hatte, C., Lang, A., Tissoux, H., Zöller, L., 2009. Rapid and cyclic Aeolian deposition during the Late Glacial in European loess: a high-resolution record from Nussloch, Germany. Quat. Sci. Rev. 28, 2955–2973.
Antoine, P., Coutard, S., Guérin, G., Descodt, L., Goval, E., Locht, J.-L., Paris, C., 2016. Upper Pleistocene loess-palaeosol records from Northern France in the European context: environmental background and dating of the Middle Palaeolithic. Quat. Int. 411, 4–24.
Bábek, O., Chlachula, J., Grygar, T.M., 2011. Non-magnetic indicators of pedogenesis related to loess magnetic enhancement and depletion: examples from the Czech Republic and southern Siberia.
Bate, S., Stevens, T., Buylaert, J.-P., Marković, S.B., Roos, P., Tasić, N., 2017. Pottery versus sediment: optically stimulated luminescence dating of the Neolithic Vinča culture, Serbia. Quat. Int. 429, 45–53.
Bateman, R.M., Catt, J.A., 2007. Provenance and palaeoenvironmental interpretation of superficial deposits, with particular reference to post-depositional modification of heavy mineral assemblages. Dev. Sedimentol. 58, 151–188.
Bateman, M.D., Boulter, C.H., Carr, A.S., Frederick, C.D., Peter, D., Wilder, M., 2007. Detecting post-depositional sediment disturbance in sandy deposits using optical luminescence. Quat. Geochronol. 2, 57–64. https://doi.org/10.1016/j.quageo.2006.05.004.
Bateman, M.D., Hitchens, S., Murton, J., Lee, J.R., Gibbard, P.L., 2014. The evolution of periglacial patterned ground in East Anglian, UK. J. Quat. Sci. 29, 301–317.
Baumgart, P., Hambach, U., Meszner, S., Faust, D., 2013. An environmental magnetic fingerprint of periglacial loess: records of Late Pleistocene loess-palaeosol sequences from Eastern Germany. Quat. Int. 296, 82–93.
Begét, J.E., Hawkins, D.B., 1989. Influence of orbital parameters on Pleistocene loess deposits in central Alaska. Nature 337, 151–153. https://doi.org/10.1038/337151a0.
Blaauw, M., Christen, J.A., 2011. Flexible paleoclimate age-depth models using an autoregressive gamma process. Bayesian Analysis 6, 457–474.
Bloemendal, J., King, J.W., Hall, F.R., Doh, S.-J., 1992. Rock magnetism of late Neogene and Pleistocene deep-sea sediments: relationship of sediment source, diagenetic processes and sediment lithology. J. Geophys. Res. 97, 4361–4375. https://doi.org/10.1029/91JB03068.
Bradák, B., Újvári, G., Seto, Y., Hyodo, M., Végh, T., 2018. A conceptual magnetic fabric development model for the Paks loess in Hungary. Aeolian Research 30, 20–31. https://doi.org/10.1016/j.aeolia.2017.11.002.
Buggle, B., Glasser, B., Hambach, U., Gerasimenko, N., Marković, S.B., 2011. An evaluation of geochemical weathering indices in loess-paleosol studies. Quat. Int. 240, 12–21.
Bullard, J.E., Baddock, M., Bradwell, T., Crusius, J., Darlington, E., Gaiero, D., Gasso, S., Gisladottir, G., Hodgkins, R., McCulloch, R., McKenna-Neuman, C., Mockford, T., Stewart, H., Thorsteinsson, T., 2016. High-latitude dust in the Earth system. Rev. Geophys. 54, 447–485. https://doi.org/10.1002/2016RG000518.
Buylaert, J.-P., Ghysels, G., Murray, A.S., Thomsen, K.J., Vandenberghe, D., De Corte, F., Heyse, I., van den Haute, P., 2009. Optical dating of relict sand wedges and composite wedge pseudomorphs in Flanders. Belgium 38, 160–175.
Buylaert, J.-P., Yeo, E.-Y., Thiel, C., Yi, S., Stevens, T., Thompson, W., Frechen, M., Murray, A., Lu, H., 2015. A detailed post-IR IRSL chronology for the last interglacial soil at the Jingbian loess site (northern China). Quat. Geochronol. 30B, 194–199. https://doi.org/10.1016/j.quageo.2015.02.022.
Catt, J.A., 1977. Loess and coversands. In: Shotton, F. (Ed.), British Quaternary Studies: Recent Advances. Clarendon Press, Oxford, pp. 221–229.
Catt, J.A., 1978. The contribution of loess to soils in lowland Britain. In: Limbrey, S., Evans, J.G. (Eds.), The Effect of Man on the Landscape: the Lowland Zone. Council for British Archaeology Research, pp. 12–20. Report 21.
Catt, J.A., 2008. Comment: new OSL dating of UK loess: indications of two phases of Late Glacial dust accretion in SE England and climate implications. J. Quat. Sci. 23, 305–306.
Catt, J.A., Staines, S.J., 1982. Loess in Cornwall. Proc. Ussher Soc. 5, 368–375.
Chiverrel, R.C., Thomas, G.S.P., Burke, M., Medialea, A., Smedley, R., Bateman, M., Clark, C., Duller, G.A.T., Fabel, D., Jenkins, G., Ou, X., Roberts, H.M., Scourse, J., 2020. The evolution of the terrestrial-terminating Irish Sea glacier during the last glaciation. J. Quat. Sci. https://doi.org/10.1002/jqs.3229. In press.
Chiverrell, R.C., Smedley, R.K., Small, D., Ballantyne, C.K., Burke, M.J., Callard, S.L., Clark, C.D., Duller, G.A.T., Evans, D.J.A., Fabel, D., van Landeghem, K., Livingstone, S., Ó Cofaigh, C., Thomas, G.S.P., Roberts, D.H., Saher, M., Scourse, J.D., Wilson, P., 2018. Ice margin oscillations during deglaciation of the northern Irish Sea basin. J. Quat. Sci. 33, 739–762.
Claquin, T., Roelandt, C., Kohfeld, K., Harrison, S., Tegen, I., Prentice, I., Balkanski, Y., Bergametti, G., Hansson, M., Mahowald, N., Rodhe, H., Schultz, M., 2003. Radiative forcing of climate by ice-age atmospheric dust. Clim. Dynam. 20, 193–202.
Clarke, M.L., Milodowski, A.E., Bouch, J.E., Leng, M.J., Northmore, K.J., 2007. New OSL dating of UK loess: indications of two phases of Late Glacial dust accretion in SE England and climate implications. J. Quat. Sci. 22, 361–371.
Clarke, M.L., Milodowski, A.E., Northmore, K.J., Leng, M.J., Bouch, J.E., 2008. Reply: evidence for episodic dust accretion in SE England. J. Quat. Sci. 23, 307–308.
COHMAP Members, 1988. Climatic changes of the last 18,000 Years: observations and model simulations. Science 241, 1043–1052.
Cullers, R.L., 2000. The geochemistry of shales, siltstones and sandstones of Pennsylvanian-Permian age, Colorado, USA: implications for provenance and metamorphic studies. Lithos 51, 181–203.
Cunningham, A.C., Wallinga, J., 2010. Selection of integration time intervals for quartz OSL decay curves. Quat. Geochronol. 5, 657–666. https://doi.org/10.1016/j.quageo.2010.08.004.
Day, R., Fuller, M., Schmidt, V.A., 1977. Hysteresis properties of titanomagnetites: grain size and composition dependence. Phys. Earth Planet. In. 13, 260–267. https://doi.org/10.1016/0031-9201(77)90108-X.
De Clercq, M., 2018. Drowned Landscapes of the Belgian Continental Shelf: Implications for Northwest European Landscape Evolution and Preservation Potential for Submerged Heritage. Unpublished PhD dissertation, Ghent University, Belgium.
Dearing, J., Dann, R.J.L., Hay, K., Lees, J.A., Loveland, P.J., Maher, B.A., O'Grady, K., 1996. Frequency-dependent susceptibility measurements if environmental materials. Geophys. J. Int. 124, 228–240.
Deng, C., Zhu, R., Verosub, K., Singer, M., Yuan, B., 2000. Paleoclimatic significance of the temperature-dependent susceptibility of Holocene loess along a NW-SE transect in the Chinese Loess Plateau. Geophys. Res. Lett. 27 (22), 3715–3718. https://doi.org/10.1029/2000GL008462.
Deng, C., Zhu, R., Jackson, M., Verosub, K., Singer, M., 2001. Variability of the temperature-dependent susceptibility of the Holocene eolian deposits in the Chinese Loess Plateau: a pedogenesis indicator. Phys. Chem. Earth Solid Earth Geodes. 26 (11-12), 873–878. https://doi.org/10.1016/S1464-1895(01)00135-1.
Dijkstra, T.A., Smalley, I.J., Rogers, C.D.F., 1995. Particle packing in loess deposits and the problem of structural collapse and hydroconsolidation. Eng. Geol. 40, 49–64.
Duller, G.A.T., 2003. Distinguishing quartz and feldspar in single grain luminescence measurements. Radiat. Meas. 37, 161–165. https://doi.org/10.1016/S1350-4487(02)00170-1.
Duller, G.A.T., 2008. Single-grain optical dating of Quaternary sediments; why aliquot size matters in luminescence dating. Boreas 37, 589–612. https://doi.org/10.1111/j.1502-3885.2008.00051.x.
Dunlop, D.J., 2002. Theory and application of the Day plot (Mrs/Ms versus Hcr/Hc) 2. Application to data for rocks, sediments, and soils. J. Geophys. Res. 107 (B3) https://doi.org/10.1029/2001JB000487.
Evans, M.E., 2001. Magnetoclimatology of aeolian sediments. Geophys. J. Int. 144, 495–497. https://doi.org/10.1046/j.0956-540X.2000.01317.x.
Evans, M.E., Heller, F., 1994. Magnetic enhancement and palaeoclimate: study of a loess/palaeosol couplet across the Loess Plateau of China. Geophys. J. Int. 117, 257–264. https://doi.org/10.1111/j.1365-246X.1994.tb03316.x.
Evans, D.J.A., Roberts, D.H., Bateman, M.D., Ely, J., Medialdea, A., Burke, M.J., Chiverrell, R.C., Clark, C.D., Fabel, D., 2019. A chronology for North Sea lobe advance and recession on the Lincolnshire and Norfolk coasts during MIS 2 and 6. PGA (Proc. Geol. Assoc.) 130, 523–540.
Fischer, P., Hambach, U., Klasen, N., Schulte, P., Zeeden, C., Steininger, F., Lehmkuhl, F., Gerlach, R., Radtke, U., 2017. Landscape instability at the end of MIS 3 in western Central Europe: evidence from a multi proxy study on a Loess-Palaeosol-Sequence from the eastern Lower Rhine Embayment, Germany. Quat. Int. 502, 119–136. https://doi.org/10.1016/j.quaint.2017.09.008.
Forste, T., Evans, M.E., Heller, F., 1994. The frequency dependence of low field susceptibility in loess sediments. Geophys. J. Int. 118, 636–642.
Fukuma, K., Torii, M., 1998. Variable shape of magnetic hysteresis loops in the Chinese loess-paleosol sequences. Earth Planets Space 50, 9–14. https://doi.org/10.1186/BF03352081.
Gao, X., Hao, Q., Oldfield, F., Bloemendal, J., Deng, C., Wang, L., Song, Y., Ge, J., Wu, H., Xu, B., Li, F., Han, L., Fu, Y., Guo, Z., 2019. New high-temperature dependence of magnetic susceptibility-based climofunction for quantifying paleoprecipitation from Chinese loess. G-cubed 20, 4273–4291. https://doi.org/10.1029/2019GC008401.
García-Moreno, D., 2017. Origin and Geomorphology of Dover Strait and Southern North Sea Palaeovalleys and Palaeodepressions. Unpublished PhD Dissertation. Ghent University, Belgium.
García-Moreno, D., Gupta, S., Collier, J.S., Oggioni, F., Vanneste, K., Trentesaux, A., Verbeek, K., Versteeg, W., Jomard, H., Camelbeeck, T., De Batist, M., 2019. Middle-Late Pleistocene landscape evolution of the Dover Strait inferred from buried and submerged erosional landforms. Quat. Sci. Rev. 203, 209–232.
Gibbard, P.L., Wintle, A.G., Catt, J.A., 1987. Age and origin of clayey silt 'brickearth' in west London. J. Quat. Sci. 2, 3–10.
Gocke, M., Hambach, U., Eckmeier, E., Schwark, L., Zöller, L., Fuchs, M., Löscher, M., Wiesenberg, G.L.B., 2014. Introducing an improved multi-proxy approach for paleoenvironmental reconstruction of loess-paleosol archives applied on the Late Pleistocene Nussloch sequence (SW Germany). Palaeogeogr. Palaeoclimatol. Palaeoecol. 410, 300–315.
Guérin, G., Mercier, N., Adamiec, G., 2011. Dose rate conversion factors: update. Ancient TL 29, 5–8.
Guérin, G., Antoine, P., Schmidt, E., Goval, E., Hérisson, D., Jamet, G., Reyss, J.-L., Shao, Q., Philippe, A., Vibet, M.-A., Bahain, J.-J., 2017. Chronology of the Upper Pleistocene loess sequence of Havrincourt (France) and associated Palaeolithic occupations: a Bayesian approach from pedostratigraphy, OSL, radiocarbon, TL and ESR/U-series data. Quat. Geochronol. 42, 15–30.
Haapaniemi, A.I., Scourse, J.D., Peck, V.L., Kennedy, H., Kennedy, P., Hemming, S.R., Furze, M.F., Pieńkowski, A.J., Austin, W.E., Walden, J., Wadsworth, E., 2010. Source, timing, frequency and flux of ice-rafted detritus to the Northeast Atlantic margin, 30-12 ka: testing the Heinrich precursor hypothesis. Boreas 39, 576–591.
Heinrich, H., 1988. Origin and consequences of cyclic ice rafting in the northeast

Atlantic Ocean during the past 130,000 years. Quat. Res. 29 (2), 142–152. https://doi:10.1016/0033-5894(88)90057-9.
Hemming, S.R., 2004. Heinrich events: massive late Pleistocene detritus layers of the North Atlantic and their global climate impact. Rev. Geophys. 42, RG1005.
Hibbert, F.D., Austin, W.E.N., Leng, M.J., Gatliff, R.W., 2009. British Ice Sheet dynamics inferred from North Atlantic ice-rafted debris records spanning the last 175 000 years. J. Quat. Sci. 25, 461–482.
Hovan, S.A., Rea, D.K., Pisias, N.G., Schackleton, N.J., 1989. A direct link between the Chinese loess and marine $\delta^{18}O$ records: aeolian flux to the north Pacific. Nature 340, 296–298.
Hrouda, F., 2011. Models of frequency-dependent susceptibility of rocks and soils revisited and broadened. Geophys. J. Int. 187, 1259–1269. https://doi.org/10.1111/j.1365-246X.2011.05227.x.
Hughes, A.L.C., Gyllencreutz, R., Lohne, Ø.S., Mangerud, J., Svendsen, J.I., 2016. The last Eurasian ice sheets – a chronological database and time-slice reconstruction, DATED-1. Boreas 45, 1–45.
Kang, S., Roberts, H.M., Wang, X., An, Z., Wang, M., 2015. Mass accumulation rate changes in Chinese loess during MIS 2, and asynchrony with records from Greenland ice cores and North Pacific Ocean sediments during the Last Glacial Maximum. Aeolian Research 19, 251–258.
Kerney, M.P., 1965. Weichselian deposits of the Isle of Thanet, East Kent. PGA (Proc. Geol. Assoc.) 76, 269–274.
King, J., Banerjee, S.K., Marvin, J., Özdemir, Ö., 1982. A comparison of different magnetic methods for determining the relative grain size of magnetite in natural materials: some results from lake sediments. Earth Planet Sci. Lett. 59, 404–419. https://doi.org/10.1016/0012-821X(82)90142-X.
Knutz, P.C., Austin, W.E.N., John W Jones, E., 2001. Millennial-scale depositional cycles related to British ice sheet variability and North Atlantic paleocirculation since 45 kyr B.P., Barra Fan, U.K. margin. Paleoceanography 16, 53–64.
Knutz, P.C., Hall, I.R., Zahn, R., Rasmussen, T.L., Kuijpers, A., Moros, M., Shackleton, N.J., 2002. Multidecadal ocean variability and NW European ice sheet surges during the last deglaciation. G-cubed 3, 1077.
Kohfeld, K., Harrison, S.P., 2003. Glacial-interglacial changes in dust deposition on the Chinese Loess Plateau. Quat. Sci. Rev. 22, 1859–1878.
Kokelj, S.V., Smith, C.A.S., Burn, C.R., 2002. Physical and chemical characteristics of the active layer and permafrost, Herschel Island, western Arctic coast, Canada. Permafr. Periglac. Process. 13, 171–185.
Krinner, G., Mangerud, J., Jakobsson, M., Crucifix, M., Ritz, C., Svendsen, J.I., 2004. Enhanced ice sheet growth in Eurasia owing to adjacent ice-dammed lakes. Nature 427, 429–432.
Lagroix, F., Banerjee, S.K., 2002. Paleowind direction from the magnetic fabric of loess profile in central Alaska. Earth Planet Sci. Lett. 195, 99–102. https://doi.org/10.1016/S0012-821X(01)00564-7.
Lefort, J.-P., Monnier, J.-L., Danukalova, G., 2019. Transport of Late Pleistocene loess particles by katabatic winds during the lowstands of the English Channel. J. Geol. Soc. 176, 1169–1181. https://doi.org/10.1144/jgs2019-070.
Leonhardt, R., 2006. Analyzing rock magnetic measurements: the RockMagAnalyzer 1.0 software. Comput. Geosci. 32, 1420–1431. https://doi.org/10.1016/j.cageo.2006.01.006.
Li, G., Xia, D., Appel, E., Wang, Y., Jia, J., Yang, X., 2018. A paleomagnetic record in loess–paleosol sequences since late Pleistocene in the arid Central Asia. Earth Planets Space 70, 44. https://doi.org/10.1186/s40623-018-0814-8.
Lill, G.O., Smalley, I.J., 1978. Distribution of loess in Britain. PGA (Proc. Geol. Assoc.) 89, 57–65.
Liu, X., Shaw, J., Liu, T., Heller, F., Yuan, B., 1992. Magnetic mineralogy of Chinese loess and its significance. Geophys. J. Int. 108, 301–308. https://doi.org/10.1111/j.1365-246X.1992.tb00859.x.
Liu, X.M., Shaw, J., Jiang, J.Z., Bloemendal, J., Hesse, P., Rolph, T., Mao, X.G., 2010. Analysis on variety and characteristics of maghemite. Sci. China Earth Sci. 53, 1–6. https://doi.org/10.1007/s11430-010-0030-2.
Loveday, J., 1962. Plateau deposits of the Chiltern Hills. Proc. Geologists' Assoc. 73, 83–102.
Lu, H., Yi, S., Liu, Z., Mason, J.A., Jiang, D., Cheng, J., Stevens, T., Xu, Z., Zhang, E., Jin, L., Zhang, Z., Guo, Z., Wang, Y., Otto-Bliesner, B., 2013. Variation of East Asian Monsoon precipitation during the past 21 k.y. and potential CO_2 forcing. Geology 41, 1023–1026. https://doi.org/10.1130/G34488.1.
Ludwig, P., Schaffernicht, E.J., Shao, Y., Pinto, J.G., 2016. Regional atmospheric circulation over Europe during the last glacial maximum and its links to precipitation. J. Geophys. Res. Atmos. 121, 2130–2145.
Maher, B.A., 2011. The magnetic properties of Quaternary aeolian dusts and sediments, and their palaeoclimatic significance. Aeolian Research 3, 87–144. https://doi.org/10.1016/j.aeolia.2011.01.005.
Maher, B.A., 2016. Palaeoclimatic records of the loess/palaeosol sequences of the Chinese Loess Plateau. Quat. Sci. Rev. 154, 23–84. https://doi.org/10.1016/j.quascirev.2016.08.004.
Maher, B.A., Taylor, R.M., 1988. Formation of ultrafine-grained magnetite in soils. Nature 336, 368–370. https://doi.org/10.1038/336368a0.
Milodowski, A.E., Northmore, K.J., Kemp, S.J., Entwistle, D.C., Gunn, D.A., Jackson, P.D., Boardman, D.I., Zoumpakis, A., Rogers, C.D.F., Dixon, N., Jefferson, I., Smalley, I.J., Clarke, M., 2015. The mineralogy and fabric of 'Brickearths' in Kent, UK and their relationship to engineering behaviour. Bull. Eng. Geol. Environ. 74, 1187–1211.
Moine, O., Antoine, P., Hatté, C., Landais, A., Mathieu, J., Prud'homme, C., Rousseau, D.-D., 2017. The impact of last glacial climate variability in west-European loess revealed by radiocarbon dating of fossil earthworm granules. Proc. Natl. Acad. Sci. Unit. States Am. 114, 6209–6214.
Moskowitz, B.M., 1981. Methods for estimating Curie temperatures of titanomagnetites from experimental Js-*T* data. Earth Planet Sci. Lett. 53, 84–88.
Murray, A.S., Wintle, A.G., 2000. Luminescence dating of quartz using an improved single-aliquot regenerative-dose protocol. Radiat. Meas. 32, 57–73. https://doi.org/10.1016/S1350-4487(99)00253-X.
Murray, A.S., Wintle, A.G., 2003. The single aliquot regenerative dose protocol: potential for improvements in reliability. Radiat. Meas. 37, 377–381. https://doi.org/10.1016/S1350-4487(03)00053-2.
Murton, J.B., Ballantyne, C.K., 2017. Periglacial and permafrost ground models for Great Britain. In: Griffiths, J.S., Martin, C.J. (Eds.), Engineering Geology and Geomorphology of Glaciated and Periglaciated Terrains – Engineering Group Working Party Report, vol. 28. Geological Society, London, Engineering Geology Special Publications, pp. 501–597.
Murton, J.A., Bateman, M.D., Baker, C.A., Knox, R., Whiteman, C.A., 2003. The devensian periglacial record on Thanet, kent, UK. Permafr. Periglac. Process. 14, 217–246.
Nawrocki, J., Gozhik, P., Łanczont, M., Pańczyk, M., Komar, M., Bogucki, A., Williams, I.S., Czupyt, Z., 2018. Palaeowind directions and sources of detrital material archived in the Roxolany loess section (southern Ukraine). Palaeogeogr. Palaeoclimatol. Palaeoecol. 496, 121–135. https://doi.org/10.1016/j.palaeo.2018.01.028.
Necula, C., Panaiotu, C., 2012. Rock magnetic properties of a loess-paleosols complex from Mircea Voda (Romania). Rom. Rep. Phys. 64 (2), 516–527.
Necula, C., Dimofte, D., Panaiotu, C., 2015. Rock magnetism of a loess-palaeosol sequence from the western Black Sea shore (Romania). Geophys. J. Int. 202, 1733–1748. https://doi.org/10.1093/gji/ggv250.
Nesbitt, H.W., Young, G.M., 1982. Early Proterozoic climates and plate motions inferred from major element chemistry of lutites. Nature 299, 715–717.
Northmore, K.J., Bell, F.G., Culshaw, M.G., 1996. The engineering properties and behaviour of the brickearth of south Essex. Q. J. Eng. Geol. Hydrogeol. 29, 147–161.
Ó Cofaigh, C., Weilbach, K., Lloyd, J.M., Benetti, S., Callard, S.L., Purcell, C., Chiverrell, R.C., Dunlop, P., Saher, M., Livingstone, S.J., Van Landeghem, K.J.J., Moreton, S.G., Clark, C.D., Fabel, D., 2019. Early deglaciation of the British-Irish Ice Sheet on the Atlantic shelf northwest of Ireland driven by glacioisostatic depression and high relative sea level. Quat. Sci. Rev. 208, 76–96.
Opdyke, N.D., Channell, J.E.T., 1996. Magnetic parameters sensitive to concentration, grain size and mineralogy. In: Magnetic Stratigraphy. Academic, USA, pp. 251–253.
Pan, Y., Zhu, R., Liu, Q., Guo, B., Yue, L., Wu, H., 2002. Geomagnetic episodes of the last 1.2 Myr recorded in Chinese loess. Geophys. Res. Lett. 29, 123-1–123-4. https://doi.org/10.1029/2001GL014024.
Parks, D.A., Rendell, H.M., 1992. Thermoluminescence dating and geochemistry of loessic deposits in south-east England. J. Quat. Sci. 7, 99–107.
Patton, H., Hubbard, A., Andreassen, K., Auriac, A., Whitehouse, P.L., Stroeven, A.P., Shackleton, C., Winsborrow, M., Heyman, J., Hall, A.M., 2017. Deglaciation of the Eurasian ice sheet complex. Quat. Sci. Rev. 169, 148–172.
Peck, V.L., Hall, I.R., Zahn, R., Elderfield, H., Grousset, F., Hemming, S.R., Scourse, J.D., 2006. High resolution evidence for linkages between NW European ice sheet instability and Atlantic Meridional Overturning Circulation. Earth Planet Sci. Lett. 243, 476–488.
Peck, V.L., Hall, I.R., Zahn, R., Grousset, F., Hemming, S.R., Scourse, J.D., 2007. The relationship of Heinrich events and their European precursors over the past 60 ka BP: a multi-proxy ice-rafted debris provenance study in the North East Atlantic. Quat. Sci. Rev. 26, 862–875.
Peric, Z., Lagerbäck Adolphi, E., Stevens, T., Ujvari, G., Zeeden, C., Buylaert, J.P., Markovic, S.B., Hambach, U., Fischer, P., Schmidt, C., Schulte, P., Huayu, L., Shuangwen, Y., Lehmkuhl, F., Obreht, I., Veres, D., Thiel, C., Frechen, M., Jain, M., Vött, A., Zöller, L., Gavrilov, M.B., 2019. Quartz OSL dating of late quaternary Chinese and Serbian loess: a cross Eurasian comparison of dust mass accumulation rates. Quat. Int. 502A, 30–44. https://doi.org/10.1016/j.quaint.2018.01.010.
Perrin, R.M.S., Davies, H., Fysh, M.D., 1974. Distribution of late Pleistocene Aeolian deposits in eastern and southern England. Nature 248, 320–324.
Pinto, J.G., Ludwig, P., 2020. Extratropical cyclones over the north Atlantic and western Europe during the last glacial maximum and implications for proxy interpretation. Clim. Past 16, 611–626.
Pitcher, W.S., Shearman, V.F., Pugh, D.C., 1954. The loess of Pegwell Bay and its associated frost soils. Geol. Mag. 91, 308–314.
Porat, N., Faerstein, G., Medialdea, A., Murray, A.S., 2015. Re-examination of common extraction and purification methods of quartz and feldspar for luminescence dating. Ancient TL 33, 22–30.
Prescott, J.R., Hutton, J.T., 1994. Cosmic ray contributions to dose rates for luminescence and ESR dating: large depths and long-term variations. Radiat. Meas. 23, 497–500.
Rasmussen, S.O., Bigler, M., Blockley, S.P., Blunier, T., Buchardt, S.L., Clausen, H.B., Cvijanovic, I., Dahl-Jensen, D., Johnsen, S.J., Fischer, H., Gkinis, V., Guillevic, M., Hoek, W.Z., Lowe, J.J., Pedro, J.B., Popp, T., Seierstad, I.K., Steffensen, J.P., Svensson, A.M., Vallelonga, P., Vinther, B.M., Walker, M.J.C., Wheatley, J.J., Winstrup, M., 2014. A stratigraphic framework for abrupt climate changes during the Last Glacial period based on three synchronized Greenland ice-core records: refining and extending the INTIMATE event stratigraphy. Quat. Sci. Rev. 106, 14–28. https://doi.org/10.1016/j.quascirev.2014.09.007.
Roberts, H.M., 2008. The development and application of luminescence dating to

loess deposits: a perspective on the past, present and future. Boreas 37, 483–507. https://doi.org/10.1111/j.1502-3885.2008.00057.x.
Roberts, A.P., Almeida, T.P., Church, N.S., Harrison, R.J., Heslop, D., Li, Y., Li, J., Muxworthy, A.R., Williams, W., Zhao, X., 2017. Resolving the origin of pseudo-single domain magnetic behaviour. J. Geophys. Res.: Solid Earth 122, 9534–9558. https://doi.org/10.1002/2017JB014860.
Roberts, D.H., Evans, D.J.A., Callard, S.L., Clark, C.D., Bateman, M.D., Medialdea, A., Dove, D., Cotterill, C.J., Saher, M., Ó Cofaigh, C., Chiverrell, R.C., Moreton, S.G., Fabel, D., Bradwell, T., 2018. Ice marginal dynamics of the last British-Irish ice sheet in the Southern North sea: ice limits, timing and the influence if the dogger bank. Quat. Sci. Rev. 198, 181–207.
Rose, J., Lee, J.A., Kemp, R.A., Harding, P.A., 2000. Palaeoclimate, sedimentation and soil development during the last glacial stage (devensian), Heathrow Airport, London, UK. Quat. Sci. Rev. 19, 827–847.
Schaetzl, R.J., Bettis, E.A., Crouvi, O., Fitzsimmons, K.E., Grimley, D.A., Hambach, U., Lehmkuhl, F., Markovic, S.B., Mason, J.A., Owraek, P., Roberts, H.M., Rousseau, D.-D., Stevens, T., Vandenberghe, J., Zarete, M., Veres, D., Yang, S., Zech, M., Conroy, J.L., Dave, A.K., Faust, D., Hao, Q., Obreht, I., Prud'homme, C., Smalley, I., Tripaldi, A., Zeeden, C., Zech, R., 2018. Approaches and challenges to the study of loess – Introduction to the LoessFest special Issue. Quat. Res. 89, 563–618. https://doi.org/10.1017/qua.2018.15.
Schaffernicht, E.J., Ludwig, P., Shao, Y., 2020. Linkage between dust cycle and loess of the last glacial maximum in Europe. Atmos. Chem. Phys. 20, 4969–4986.
Scourse, J.D., 1991. Late Pleistocene stratigraphy and palaeobotany of the Isles of Scilly. Phil. Trans. Roy. Soc. Lond. B 334, 405–448.
Scourse, J.D., Haapaniemi, A.I., Colmenero-Hidalgo, E., Peck, V.L., Hall, I.R., Austin, W.E., Knutz, P.C., Zahn, R., 2009. Growth, dynamics and deglaciation of the last British-Irish ice sheet: the deep-sea ice-rafted detritus record. Quat. Sci. Rev. 28, 3066–3084.
Scourse, J., Sher, M., Van Langdeghem, K.J.J., Lockhart, E., Purcell, C., Callard, L., Roseby, Z., Allinson, B., Pieńkowski, A.J., O'Cofaigh, C., Praeg, D., Ward, S., Chiverrell, R., Moreton, S., Fabel, D., Clark, C.D., 2019. Advance and retreat of the marine-terminating Irish sea ice stream into the Celtic sea during the last glacial: timing and maximum extent. Mar. Geol. 412, 53–68.
Sechi, D., Andreucci, S., Stevens, T., Pascucci, V., 2020. Age and significance of late Pleistocene Lithophyllum byssoides intertidal algal ridge, NW Sardinia, Italy. Sediment. Geol. 400, 105618.
Seelos, C., Sirocko, F., Dietrich, S., 2009. A continuous high-resolution dust record for the reconstruction of wind systems in central Europe (Eifel, Western Germany) over the past 133 ka. Geophys. Res. Lett. 36, L20712.
Seguinot, J., Ivy-Ochs, S., Jouvet, g., Huss, M., Funk, M., Preusser, F., 2018. Modelling last glacial cycle ice dynamics in the Alps. Cryosphere 12, 3265–3285. https://doi.org/10.5194/tc-12-3265-2018.
Sima, A., Rousseau, D.-D., Kageyama, M., Ramstein, G., Schultz, M., Balkanski, Y., Antoine, P., Dulac, F., Hatté, C., 2009. Imprint of North-Atlantic abrupt climate changes on western European loess deposits as viewed in a dust emission model. Quat. Sci. Rev. 28, 2851–2866.
Smalley, I.J., Marković, S.B., 2014. Loessification and hydroconsolidation. There is a connection. Catena 94–99.
Smalley, I.J., O'Hara-Dhand, K., Wint, J., Machalett, B., Jary, Z., Jefferson, I., 2009. Rivers and loess: the significance of long river transportation in the complex event-sequence approach to loess deposit formation. Quat. Int. 198, 7–18.
Smedley, R.K., Scourse, J.D., Small, D., Hiemstra, H.F., Duller, G.A.T., Bateman, M.D., Burke, M.J., Chiverrell, R.C., Clark, C.D., Davies, S.M., Fabel, D., Gheorghiu, D.M., McCarroll, D., Medialdea, A., Xu, S., 2017. New age constraints for the limit of the British-Irish ice sheet on the Isles of Scilly. J. Quat. Sci. 32, 48–62.
Stevens, T., 2019. Applications in loesssic environments. In: Bateman, M. (Ed.), Handbook of Luminescence Dating, Whittles, UK, pp. 153–190.
Stevens, T., Armitage, S.J., Lu, H., Thomas, D.S.G., 2007. Examining the potential of high-resolution OSL dating of Chinese loess. Quat. Geochronol. 2, 15–22.
Stevens, T., Lu, H., Thomas, D.S.G., Armitage, S.J., 2008. Optical dating of abrupt shifts in the late Pleistocene east asian monsoon. Geology 36, 415–418. https://doi.org/10.1130/G24524A.1.
Stevens, T., Marković, S.B., Zech, M., Sümegi, P., 2011. Dust deposition and climate in the Carpathian Basin over an independently dated last glacial-interglacial cycle. Quat. Sci. Rev. 30, 662–681.
Stevens, T., Buylaert, J.-P., Lu, H., Thiel, C., Murray, A., Frechen, M., Yi, S., Lin, Z., 2016. Mass accumulation rate and monsoon records from Xifeng, Chinese Loess Plateau, based on a luminescence age model. J. Quat. Sci. 31, 391–405. https://doi.org/10.1002/jqs.2848.
Stevens, T., Buylaert, J.-P., Thiel, C., Újvári, G., Yi, S., Murray, A.S., Frechen, M., Lu, H., 2018. Ice-volume-forced erosion of the Chinese Loess Plateau global Quaternary stratotype site. Nat. Commun. 9, 983. https://doi.org/10.1038/s41467-018-03329-2.
Stroeven, A.P., Hätterstrand, C., Kleman, J., Heyman, J., Fabel, D., Fredin, O., Goodfellow, B.W., Harbor, J.M., Jansen, J.D., Olsen, L., Caffee, M.W., Fink, D., Lundqvist, J., Rosqvist, G.C., Strömberg, B., Jansson, K.N., 2016. Deglaciation of fennoscandia. Quat. Sci. Rev. 147, 91–121.
Sun, Y., Clemens, S.C., Morrill, C., Lin, X., Wang, X., An, Z., 2011. Influence of Atlantic meridional overturning circulation on the East Asian winter monsoon. Nat. Geosci. 5, 46–49.
Taylor, S.N., Lagroix, F., Rousseau, D.-D., Antoine, P., 2014. Mineral magnetic characterization of the Upper Pleniglacial Nussloch loess sequence (Germany): an insight into local environmental processes. Geophys. J. Int. 199, 1463–1480. https://doi.org/10.1093/gji/ggu331.
Thomsen, K.J., Murray, A.S., Buylaert, J.-P., Jain, M., Hansen, J.H., Aubry, T., 2016. Testing single-grain quartz OSL methods using sediment samples with independent age control from the Bordes-Fitterockshelter (Roches d'Abilly site, Central France). Quat. Geochronol. 31, 77–79. https://doi.org/10.1016/j.quageo.2015.11.002.
Timar-Gabor, A., Buylaert, J.-P., Guralnik, B., Trandafir-Antohi, O., Constantin, D., Anechitei-Deacu, V., Jain, M., Murray, A.S., Porat, N., Hao, Q., Wintle, A.G., 2017. On the importance of grain-size in luminescence dating using quartz. Radiat. Meas. 106, 464–471.
Toucanne, S., Soulet, G., Freslon, N., Jacinto, R.S., Dennielou, B., Zaragosi, S., Eynaud, F., Bourillet, J.-F., Bayon, G., 2015. Millennial-scale fluctuations of the European Ice Sheet at the end of the last glacial, and their potential impact on global climate. Quat. Sci. Rev. 123, 113–133. https://doi.org/10.1016/j.quascirev.2015.06.010.
Trachsel, M., Telford, R.J., 2017. All age models are wrong, but are getting better. Holocene 27, 860–869.
Újvári, G., Kovács, J., Varga, G., Raucsik, B., Marković, S.B., 2010. Dust flux estimates for the Last Glacial Period in East Central Europe based on terrestrial records of loess deposits: a review. Quat. Sci. Rev. 29, 3157–3166.
Újvári, G., Varga, A., Ramos, F.C., Kovács, J., Németh, T., Stevens, T., 2012. Evaluating the use of clay mineralogy, Sr–Nd isotopes and zircon U–Pb ages in tracking dust provenance: an example from loess of the Carpathian Basin. Chem. Geol. 304 (305), 83–96. https://doi.org/10.1016/j.chemgeo.2012.02.007.
Újvári, G., Kok, J.F., Varga, G., Kovács, J., 2016. The physics of wind-blown loess: implications for grain size proxy interpretations in Quaternary palaeoclimate studies. Earth Sci. Rev. 154, 247–278.
Újvári, G., Stevens, T., Molnar, M., Demeny, A., Varga, G., Lambert, F., Jull, A.J.T., Pall-Gergely, B., Buylaert, J.-P., Kovacs, J., 2017. Coupled European and Greenland last glacial dust activity driven by North Atlantic climate. Proc. Natl. Acad. Sci. Unit. States Am. 114, E10632–E10638. https://doi.org/10.1073/pnas.1712651114.
Vandenberghe, J., 2013. Grain size of fine-grained windblown sediment: a powerful proxy for process identification. Earth Sci. Rev. 121, 18–30.
Vandenberghe, J., Nugteren, G., 2001. Rapid climatic changes recorded in loess successions. Global Planet. Change 28, 1–9.
Vandenberghe, D., De Corte, F., Buylaert, J.-P., Kučera, J., Van den haute, P., 2008. On the internal radioactivity in quartz. Radiat. Meas. 43, 771–775.
Weir, A.H., Catt, J.A., Madgett, P.A., 1971. Postglacial soil formation in the loess of Pegwell Bay, kent (England). Geoderma 5, 131–149.
Wintle, A.G., 1981. Thermoluminescence dating of late Devensian loesses in southern England. Nature 289, 479–480.
Wintle, A.G., Catt, J.A., 1985. Thermoluminescence dating of soils developed in late devensian loess at Pegwell Bay, kent. J. Soil Sci. 36, 293–298.
Wintle, A.G., Murray, A.S., 2006. A review of quartz optically stimulated luminescence characteristics and their relevance in single-aliquot regeneration dating protocols. Radiat. Meas. 41, 369–391. https://doi.org/10.1016/j.radmeas.2005.11.001.
Yi, S., Buylaert, J.P., Murray, A.S., Lu, H., Thiel, C., Zeng, L., 2016. A detailed post-IR IRSL dating study of the Niuyangzigou loess site in northeastern China. Boreas 45 (4), 644–657. https://doi.org/10.1111/bor.12185.
Zeeden, C., Kels, H., Hambach, U., Schulte, P., Protze, J., Eckmeier, E., Marković, S.B., Klasen, N., Lehmkuhl, F., 2016. Three climatic cycles recorded in a loess-palaeosol seuqnce at Semlac (Romania) – implications for dust accumulation in south-eastern Europe. Quat. Sci. Rev. 154, 130–142.
Zeeden, C., Hambach, U., Veres, D., Fitzsimmons, K., Obreht, I., Bösken, J., Lehmkuhl, F., 2018. Millennial scale climate oscillations recorded in the Lower Danube loess over the last glacial period. Palaeogeogr. Palaeoclimatol. Palaeoecol. 509, 164–181.
Zens, J., Schulte, P., Klasen, N., Krauss Pirson, S., Burow, C., Brill, D., Eckmeier, E., Kels, H., Zeeden, C., Spagna, P., Lehmkuhl, F., 2018. OSL chronologies of paleo-environmental dynamics recorded by loess-paleosol sequences from Europe: case studies from the Rhine-Meuse area and the Neckar Basin. Palaeogeography, Palaeclimatology, Palaeoecology 509 105–125.
Zhu, R., Deng, C., Jackson, M.J., 2001. A magnetic investigation along a NW-SE transect of the Chinese Loess Plateau and its implications. Phys. Chem. Earth Solid Earth Geodes. 26 (11-12), 867–872. https://doi.org/10.1016/S1464-1895(01)00134-X.